

# 000 001 002 003 004 005 006 007 008 009 010 011 012 013 014 015 016 017 018 019 020 021 022 023 024 025 026 027 028 029 030 031 032 033 034 035 036 037 038 039 040 041 042 043 044 045 046 047 048 049 050 051 052 053 LEARNING CONCEPT BOTTLENECK MODELS FROM MECHANISTIC EXPLANATIONS

Anonymous authors

Paper under double-blind review

## ABSTRACT

Concept Bottleneck Models (CBMs) aim for ante-hoc interpretability by learning a bottleneck layer that predicts interpretable concepts before the decision. State-of-the-art approaches typically select which concepts to learn via human specification, open knowledge graphs, prompting an LLM, or using general CLIP concepts. However, concepts defined a-priori may not have sufficient predictive power for the task or even be learnable from the available data. As a result, these CBMs often significantly trail their black-box counterpart when controlling for information leakage. To address this, we introduce a novel CBM pipeline named Mechanistic CBM (M-CBM), which builds the bottleneck directly from a black-box model’s own learned concepts. These concepts are extracted via Sparse Autoencoders (SAEs) and subsequently named and annotated on a selected subset of images using a Multimodal LLM. For fair comparison and leakage control, we also introduce the Number of Contributing Concepts (NCC), a decision-level sparsity metric that extends the recently proposed NEC metric. Across diverse datasets, we show that M-CBMs consistently surpass prior CBMs at matched sparsity, while improving concept predictions and providing concise explanations. Our code is available at <https://anonymous.4open.science/r/M-CBM-85D9>.

## 1 INTRODUCTION

As AI systems become increasingly complex and embedded in high-stakes applications such as healthcare, autonomous driving, and defense, there is a growing demand for vision models that not only perform well but are also transparent and interpretable. To obtain explanations for AI decisions, we can generally take two approaches: (i) utilize post-hoc methods that try to gain insights into how black-box models produce their outputs, or (ii) develop inherently transparent models that can explain their decisions by design (i.e., ante-hoc explainability) (Xu et al., 2019). In computer vision, a promising ante-hoc approach to explainability are Concept Bottleneck Models (CBMs), which are trained to first predict an intermediate set of interpretable concepts and then use these concepts to predict the final output. Recent practice typically instantiates this concept set a-priori, either specified by human experts (Koh et al., 2020), based on knowledge graphs (Yuksekgonul et al., 2023), by prompting an LLM (Yang et al., 2023; Oikarinen et al., 2023; Srivastava et al., 2024), or using general concepts from pre-trained vision-language models (Rao et al., 2024). However, concepts defined a-priori may not have sufficient predictive power for the target task or even be learnable from the available data. As a result, state-of-the-art CBMs substantially underperform their black-box counterpart when controlling for information leakage. Beyond performance, a further reason not to fix concepts a-priori is that modern ML systems often equal or exceed human expertise, creating an opportunity to use interpretability to learn from machines. For example, Schut et al. (2025) extracted concepts learned by the chess engine AlphaZero (Silver et al., 2017) and were able to teach them to grandmasters. Furthermore, mechanistic interpretability has recently made significant progress in comprehensively extracting concepts from black-box models, in particular via Sparse Autoencoders (SAEs) (Bricken et al., 2023). Motivated by this, we ask whether CBMs built directly from a model’s own learned concepts can serve as interpretable approximations of their black-box counterparts. Because these concepts originate in the backbone, we expect them to be learnable by construction and to have good predictive power. To test this, we develop a novel CBM pipeline, which we refer to as Mechanistic CBM (M-CBM), and compare it to state-of-the-art CBMs in both task accuracy and its ability to learn concepts, showing significant improvements.

054 **2 RELATED WORK**

055

056 **Concept-based Explanations.** Early approaches for explainable computer vision typically rely  
 057 on saliency (Selvaraju et al., 2017) or attribution maps (Sundararajan et al., 2017) that show which  
 058 regions or pixels of an image contribute the most to a decision. By contrast, concept-based methods  
 059 aim to provide explanations in terms of higher-level, human-understandable concepts (e.g., stripes  
 060 for a zebra). A seminal contribution to the field was TCAV (Kim et al., 2018), a method that in-  
 061 vestigates a model’s sensitivity to a user-defined concept by collecting a set of example images  
 062 representing that concept. Later, De Santis et al. (2025) extended TCAV with per-instance concept  
 063 attributions and saliency maps indicating where the concept is recognized. However, both of these  
 064 methods have practical limitations as they require users to manually collect concept examples. To  
 065 address this, unsupervised approaches have also been proposed (Ghorbani et al., 2019; Zhang et al.,  
 066 2021; Fel et al., 2023) to automatically discover influential concepts for a given class. These meth-  
 067 ods typically crop images of a class, randomly or via segmentation, and cluster the cropped patch  
 068 activations to extract groups of semantically similar patches that correspond to a concept. However,  
 069 with this approach, achieving completeness (i.e., extracting a concept set sufficient to recover the  
 070 model’s prediction) remains a nontrivial task (Yeh et al., 2020).

071 **Mechanistic Interpretability.** Mechanistic interpretability (MI) aims to comprehensively *reverse-*  
 072 *engineer* deep networks by converting their neurons and weights into interpretable features and  
 073 algorithms, and it differentiates itself from concept-based approaches primarily for its ambition of  
 074 completeness (Bereska & Gavves, 2024). A central challenge to this is *polysemanticity*, i.e., neurons  
 075 often respond to unrelated features, so they cannot be mapped one-to-one with concepts (Olah et al.,  
 076 2020). This could allow networks to learn far more features than there are neurons, which is known  
 077 as the *superposition* hypothesis (Elhage et al., 2022). Recently, Bricken et al. (2023) showed this can  
 078 be addressed post-hoc by disentangling features via Sparse Autoencoders (SAEs) that learn a sparse,  
 079 overcomplete dictionary of monosemantic features that then reconstruct the original activations. The  
 080 SAE reconstruction error also provides a quantitative proxy for completeness in a chosen layer.  
 081 Given their effectiveness in both language (Gao et al., 2025) and vision (Gorton, 2024; Thasarathan  
 082 et al., 2025), we also adopt SAEs for concept extraction in our pipeline (see Section 3 for more  
 083 details on SAEs). Another emerging trend in MI is *automated interpretability*, i.e., using LLMs  
 084 to generate natural language explanations for reverse-engineering neuron behavior. This was first  
 085 applied to explain language model neurons (Bills et al., 2023), but then also proved effective to  
 086 explain vision models (Rott Shaham et al., 2024). We also use a similar approach to assign names  
 087 to concepts extracted via SAEs (Section 3). MI has also made progress in dissecting models into  
 088 interpretable circuits (e.g., identifying algorithmic sub-structures within deep networks) via masking  
 089 or patching procedures (Conmy et al., 2023). Those circuit-level analyses are currently not being  
 090 used in our pipeline, but integrating them could be a promising future work.

091 **Concept Bottleneck Models.** Concept Bottleneck Models (CBMs) are self-explaining neural net-  
 092 works that learn a set of intermediate human-understandable concepts to solve a task. The term  
 093 was first introduced by Koh et al. (2020), who trained CBMs using datasets with concept anno-  
 094 tations. Later, Yuksekgonul et al. (2023) relaxed this requirement with post-hoc CBMs that learn  
 095 a Concept Bottleneck Layer (CBL) using Concept Activation Vectors (CAVs) (Kim et al., 2018),  
 096 only requiring manual selection of representative examples for each concept. Furthermore, when  
 097 using a CLIP (Radford et al., 2021) backbone, it learns concepts directly from text sourced from the  
 098 ConceptNet (Speer et al., 2017) knowledge graph. Yang et al. (2023) later showed benefits in gener-  
 099 ating the concept set with LLMs. Oikarinen et al. (2023) extended this paradigm also to non-CLIP  
 100 backbones using CLIP-Dissect (Oikarinen & Weng, 2023) to map concept embeddings in CLIP to  
 101 any backbone. A known problem, however, that exists across all CBMs is *information leakage*,  
 102 i.e., the fact that the CBL inadvertently encodes hidden class-relevant patterns beyond the concept  
 103 semantics, which can be quickly learned by the final predictor to improve its accuracy (Havasi et al.,  
 104 2022b). This issue is quite serious, as Yan et al. (2023) even showed that replacing concepts with  
 105 random words can achieve similar accuracy. Information leakage also results in unsatisfying expla-  
 106 nations, in which the most important concepts contribute significantly less than the sum of all other  
 107 concepts, making the model basically a black-box. Furthermore, while for classical CBMs leakage  
 108 can at least be quantified using dedicated metrics based on ground-truth concept labels (Havasi et al.,  
 109 2022a; Zarlenga et al., 2023), for CBMs that learn concepts automatically, quantifying leakage be-

comes even more challenging. To address this, Srivastava et al. (2024) introduced the Number of Effective Concepts (NEC) as a metric to measure and control how many concepts CBMs use to make a prediction, effectively reducing information leakage. In this work, we also follow this approach and use the Number of Contributing Concepts (NCC), a generalization of NEC, to control for leakage and explanation conciseness. More details on NEC and NCC are provided in Section 4. Srivastava et al. (2024) also introduced VLG-CBM, a CBM pipeline that uses GroundingDINO (Liu et al., 2025), an open-vocabulary object detector, to automatically annotate a dataset with LLM-generated concepts. The CBL is then trained on these annotations in a multilabel setting, allowing also for the evaluation of concept predictions, similar to the vanilla CBM by Koh et al. (2020). However, leakage still arises from the annotation being class-conditioned, as we show in Section 5. Another limitation of these CBM paradigms is that LLM-generated concept sets offer no guarantees that the proposed concepts have sufficient predictive power for the target task and are even learnable from the available data, requiring the inclusion of uninterpretable components in the bottleneck to recover accuracy (Yuksekgonul et al., 2023; Zhang et al., 2025; Shang et al., 2024). Sometimes concepts can also be non-visual (Roth et al., 2023). We instead propose extracting and using the black-box model’s own learned concepts, rather than guessing with an LLM. A first step in this direction within the literature is DN-CBM (Rao et al., 2024), which learns concepts from CLIP with an SAE and uses its hidden layer as CBL, naming the concepts by selecting the nearest CLIP text embeddings to the decoder vector. However, this paradigm can only be applied with CLIP as a backbone, limiting its accuracy across datasets, as we show in Section 6. Furthermore, CLIP dependence can still introduce non-visual concepts (e.g., “spicy”, “loud”), making explanations less transparent (Srivastava et al., 2024; Yang et al., 2023).

### 3 METHODOLOGY

In this section, we introduce our methodology for transforming any black-box model into an interpretable-by-design CBM. Our approach, which we refer to as Mechanistic CBM (M-CBM), extracts human-interpretable concepts from a trained black-box model, assigns names and annotations using a Multimodal Large Language Model (MLLM), and then trains a sequential CBM (Koh et al., 2020) using these concepts. An overview of the whole pipeline is provided in Figure 1.

**Concept Extraction.** Given a black-box backbone  $\phi$  trained on an arbitrary dataset  $\mathbb{D}$ , the first step of our methodology is to decompose the features learned by the model during training into a set of interpretable concepts. To achieve this, we use the Sparse Autoencoder (SAE) approach, which was recently popularized in the mechanistic interpretability literature (Bereska & Gavves, 2024) and has proven effective to disentangle model features into interpretable concepts for both vision (Gorton, 2024; Thasarathan et al., 2025) and language models (Bricken et al., 2023; Huben et al., 2024).

An SAE is a neural network trained to reconstruct its input features while enforcing sparsity in the hidden representation (see step ① in Figure 1). In our case, the input features are the activations  $\mathbf{a}^{(i)} = \phi(\mathbf{x}^{(i)}) \in \mathbb{R}^n$  of the backbone  $\phi$  for each sample  $\mathbf{x}^{(i)}$  in the training set  $\mathbb{D}$ . Following Bricken et al. (2023), the SAE subtracts an input bias  $\mathbf{b}_D$  and then passes the resulting vector to an encoder with weights  $\mathbf{W}_E$ , bias  $\mathbf{b}_E$ , and ReLU activation, obtaining the hidden layer  $\mathbf{h} \in \mathbb{R}^m$ :

$$\mathbf{h} = \text{ReLU}(\mathbf{W}_E^\top(\mathbf{a} - \mathbf{b}_D) + \mathbf{b}_E)$$

In the sparse hidden layer  $\mathbf{h}$ , ideally, each neuron learns to recognize a distinct concept. A decoder with weights  $\mathbf{W}_D$  and bias  $\mathbf{b}_D$  then maps  $\mathbf{h}$  back to the reconstructed features  $\hat{\mathbf{a}}$ :

$$\hat{\mathbf{a}} = \mathbf{W}_D^\top \mathbf{h} + \mathbf{b}_D$$

where  $\mathbf{W}_E \in \mathbb{R}^{n \times m}$ ,  $\mathbf{W}_D \in \mathbb{R}^{m \times n}$ , and typically for large datasets  $m \gg n$  to account for the superposition hypothesis (Elhage et al., 2022), i.e., the fact that neural networks tend to learn more concepts than the neurons they have. The input and output biases  $\mathbf{b}_D$  are opposite in sign and equal in magnitude. While Bricken et al. (2023) train SAEs with expansion factors (defined as  $m/n$ ) ranging from  $1x$  to  $256x$ , we avoid going above  $4x$  to keep the annotation step computationally feasible. To train the SAE, we minimize the following objective:

$$\mathcal{L}_{\text{SAE}} = \frac{1}{|\mathbb{D}|} \sum_{i=1}^{|\mathbb{D}|} \|\mathbf{a}^{(i)} - \hat{\mathbf{a}}^{(i)}\|_2^2 + \lambda_{\text{SAE}} \|\mathbf{h}^{(i)}\|_1 \quad (1)$$

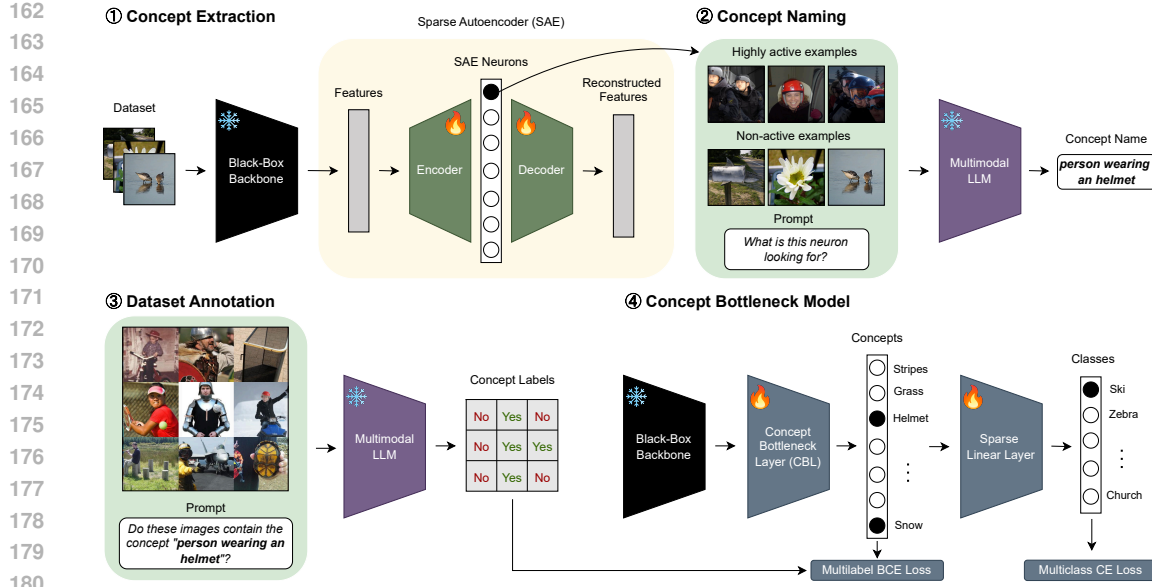


Figure 1: Overview of the M-CBM pipeline. (1) Given a trained black-box backbone, we extract its features and learn sparse, disentangled concept directions using a Sparse Autoencoder (SAE). (2) A Multimodal LLM is prompted with examples of highly activating and non-activating images to assign concept names to each SAE neuron. (3) The MLLM then annotates a subset of the dataset containing an equal split of active and non-active examples, indicating the presence or absence of each concept in selected images. (4) Using these concept annotations, we train a Concept Bottleneck Layer (CBL) and a sparse linear classifier to predict target classes from the learned concepts.

where  $\lambda_{\text{SAE}} > 0$  is a hyperparameter that controls the strength of the sparsity penalty on the hidden representation. We also monitor the average  $\ell_0$  norm (i.e., the number of non-zero activations) to ensure  $\ell_0 \ll n$ , as recommended by Bricken et al. (2023).

SAE training often leaves many neurons in the hidden layer  $\mathbf{h}$  dead (never activated for any training sample) or nearly dead (activate only very rarely). To ensure that our set of candidate concepts is both meaningful and computationally efficient for subsequent annotation, we perform a filtering step to remove such neurons. To define the threshold for identifying nearly dead neurons, we measure, for each unit in  $\mathbf{h}$ , the number of training samples for which it is active. We then select a cutoff value such that removing all units below this threshold does not reduce the recovered cross-entropy loss of the black-box model, defined as  $1 - \frac{\mathcal{L}_{\text{BB}}(\hat{\mathbf{a}}) - \mathcal{L}_{\text{BB}}(\mathbf{a})}{\mathcal{L}_{\text{BB}}(\mathbf{0}) - \mathcal{L}_{\text{BB}}(\mathbf{a})}$ , by more than a tolerance of  $\sim 1\%$ . This procedure ensures that only neurons with negligible contribution to predictive performance are pruned. This metric was also used to evaluate SAE quality in prior work (Bricken et al., 2023; Rajamanoharan et al., 2024; Gao et al., 2025). More details on SAEs in Appendix B.

**Concept Naming.** After pruning, each remaining neuron in the SAE hidden layer  $\mathbf{h}$  is treated as a candidate concept, where we denote by  $h_j$  the  $j$ -th hidden SAE neuron. To assign human-interpretable names, we adopt an automated procedure inspired by recent work on mechanistic interpretability of language model neurons (Bills et al., 2023). For each candidate concept, we first select a set of inputs  $\mathbf{x} \in \mathbb{D}$  that maximally activate the corresponding neuron  $h_j$ . For these inputs, we also highlight the spatial regions that contribute the most to the activation, similarly to Rott Shaham et al. (2024). To compute these concept saliency maps, we use the method introduced by De Santis et al. (2025) (i.e., weighted average of feature maps using  $\mathbf{W}_D$  as concept weights and followed by ReLU). To provide a contrastive signal, we additionally sample a set of non-activating examples, of which half are drawn at random from  $\mathbb{D}$ , and half are selected as the most cosine similar to the activating examples to enhance discrimination of fine-grained visual features. The paired examples are provided to an MLLM, GPT-4.1 in our experiments, which is prompted to produce a concise natural-language description of the concept that the neuron represented by  $h_j$  is responding to. At this stage, we also explicitly instruct the model not to use class names as concepts and re-try

216 if it does not adhere. Step ② of Figure 1 shows an example of what the MLLM receives as input. In  
 217 our experiments, we used 10 activating examples and 10 non-activating ones.  
 218

219 Finally, since we do not want duplicate or semantically equivalent concepts, we perform a merging  
 220 step similar to Oikarinen et al. (2023), in which we embed all proposed textual names using a pre-  
 221 trained embedding model and merge those with very high cosine similarity (i.e., above 0.98). We  
 222 use OpenAI’s *text-embedding-3-large* in our experiments. To make the embeddings context-aware,  
 223 we also wrap each concept name in the following template before inserting it into the embedding  
 224 model: “This is a visual concept in the context of  $\{domain\}$ :  $\{concept\}$ ”. The variable  $\{concept\}$   
 225 contains the concept name, while  $\{domain\}$  specifies the dataset domain (e.g., bird species, skin  
 226 lesions). For simplicity, Figure 1 omits the merging step.  
 227

228 **Dataset Annotation.** With concept names assigned, we proceed to build a partially annotated  
 229 dataset that can be used to train the Concept Bottleneck Layer (CBL). Let  $\mathbb{C} = \{c_1, \dots, c_K\}$  denote  
 230 the final set of concepts. For each concept  $c_k$ , the goal is to obtain binary presence/absence labels  
 231 on a subset of images  $\mathbf{x} \in \mathbb{D}$ . Since exhaustive annotation of the full dataset is not computationally  
 232 feasible at the time of writing this paper, we annotate up to 1000 samples per concept, drawn mainly  
 233 from the training, but also from the test set (e.g., 20-30%) solely for a final CBL evaluation (results  
 234 in Section 6). The annotation procedure is performed by prompting the MLLM with batches of 25  
 235 images arranged in a  $5 \times 5$  grid for computational efficiency. The model is asked to indicate, for  
 236 each of the 25 grid images, whether the concept is present or absent. See step ③ of Figure 1 for a  
 237 high-level overview of the annotation procedure. Each call also includes a grid of the top-25 most  
 238 activating images for the corresponding SAE neuron, which serve as a reference together with the  
 239 textual concept name.

240 To select the subset of images for annotation, we first select up to 500 active samples per concept.  
 241 The active set is defined as all inputs for which  $h_j > 0$ . From this set, we select samples whose  
 242 activation lies above the 95th percentile of the set. If fewer than 500 samples exceed this percentile,  
 243 we take the top-500 activations overall within the active set. If the neuron has fewer than 500 active  
 244 samples in total, we take all available examples, rounding the number down to the nearest multiple  
 245 of 25 to match the batch annotation protocol. For merged neurons, activations are normalized across  
 246 the group and treated as a single unit when computing percentiles. We then select an equal number  
 247 of non-active samples, of which half are drawn uniformly at random and half are chosen as the  
 248 most cosine similar to the active samples, similarly to the naming procedure. Furthermore, to avoid  
 249 biasing concepts toward particular classes, both active and non-active sets are stratified across class  
 250 labels. Each batch of 25 images also contains a balanced mix of active and non-active examples. At  
 251 the end of this annotation step, we obtain a set of around 1000 annotated samples for each concept,  
 252 containing both presence and absence cases across both training and test data. An image may be  
 253 annotated for more than one concept or for none. Formally, for each image  $\mathbf{x}^{(i)} \in \mathbb{D}$ , the annotation  
 254 procedure creates a ternary vector of concept labels  $\mathbf{z}^{(i)} \in \{-1, 0, 1\}^K$  with the following entries:  
 255

$$z_k^{(i)} = \begin{cases} 1 & \text{if } c_k \text{ is annotated as } \textit{present} \text{ in } \mathbf{x}^{(i)} \\ 0 & \text{if } c_k \text{ is annotated as } \textit{absent} \text{ in } \mathbf{x}^{(i)} \\ -1 & \text{if } c_k \text{ is not annotated for } \mathbf{x}^{(i)} \end{cases} \quad (2)$$

256 **Concept Bottleneck Model.** After generating the concept labels, we proceed with training a se-  
 257 quential CBM (Koh et al., 2020). As shown in step ④ of Figure 1, the CBM has three components:  
 258 (i) a frozen backbone  $\phi$  that maps an input image to a feature vector, (ii) a Concept Bottleneck Layer  
 259 (CBL)  $g$  that predicts the presence of  $K$  named concepts from those features in a multi-label setting,  
 260 and (iii) a sparse linear classifier  $f$  that predicts the class from the concept outputs.

261 For each input  $\mathbf{x}^{(i)}$  the frozen backbone produces  $n$ -dimensional features  $\mathbf{a}^{(i)} = \phi(\mathbf{x}^{(i)}) \in \mathbb{R}^n$ . The  
 262 CBL  $g : \mathbb{R}^n \rightarrow \mathbb{R}^K$  takes these features as input and outputs concept logits, then a sigmoid produces  
 263 probabilities  $\hat{\mathbf{z}}^{(i)} = \sigma(g(\mathbf{a}^{(i)})) \in [0, 1]^K$ . From the annotation pipeline, each image carries a  
 264 ternary concept vector  $\mathbf{z}^{(i)} \in \{-1, 0, 1\}^K$  indicating present (1), absent (0), or not annotated (-1).  
 265 Since not every image-concept pair is labeled, we train  $g$  only on the entries we know. Let  $\Omega =$   
 266  $\{(i, k) : z_k^{(i)} \in \{0, 1\}\}$  be the set of annotated pairs. The CBL is optimized to minimize a masked  
 267

270 Binary Cross-Entropy (BCE) loss that averages over  $\Omega$ :  
 271

$$\mathcal{L}_{\text{CBL}} = \frac{1}{|\Omega|} \sum_{(i,k) \in \Omega} \text{BCE}(\hat{z}_k^{(i)}, z_k^{(i)}) \quad (3)$$

275 Entries with  $z_k^{(i)} = -1$  are effectively ignored in the loss computation. Therefore, images without  
 276 any concept annotation (all entries  $-1$ ) are not used to train the CBL. Furthermore, since positives  
 277 are often rarer than negatives, we weight each concept in the BCE by the ratio of its class imbalance.  
 278

279 To map concepts to classes, we follow prior work (Srivastava et al., 2024; Yuksekgonul et al., 2023;  
 280 Oikarinen et al., 2023) and train a sparse linear classifier on concept logits (i.e., CBL’s pre-sigmoid  
 281 outputs), optimized using the GLM-SAGA solver (Wong et al., 2021). Since GLM-SAGA assumes  
 282 standardized input features, we  $z$ -normalize (zero mean and unit variance) the concept logits and  
 283 use these to predict the classes. With  $g$  frozen, we define a fully connected layer  $f : \mathbb{R}^K \rightarrow \mathbb{R}^C$  with  
 284 weights  $\mathbf{W}_F \in \mathbb{R}^{K \times C}$  and bias  $\mathbf{b}_F \in \mathbb{R}^C$ , where  $C$  is the number of output classes, and minimize  
 285 the following Cross-Entropy (CE) loss with an elastic-net (Zou & Hastie, 2005) penalty:  
 286

$$\mathcal{L}_{\text{CLF}} = \frac{1}{|\mathbb{D}|} \sum_{i=1}^{|\mathbb{D}|} \text{CE}(f \circ g \circ \phi(\mathbf{x}^{(i)}), \mathbf{y}^{(i)}) + \lambda_{\text{CLF}} R_\alpha \quad (4)$$

287 where  $\mathbf{y}^{(i)}$  represents the one-hot ground-truth class label for sample  $\mathbf{x}^{(i)}$  and  $R_\alpha = (1 -$   
 288  $\alpha) \frac{1}{2} \|\mathbf{W}_F\|_2^2 + \alpha \|\mathbf{W}_F\|_1$  denotes the elastic-net penalty. Following Wong et al. (2021), we use  
 289  $\alpha = 0.99$ , while  $\lambda_{\text{CLF}}$  is tuned to obtain a target sparsity.  
 290

## 293 4 NUMBER OF CONTRIBUTING CONCEPTS (NCC)

295 Prior work has shown that sparse layers are more interpretable (Wong et al., 2021; Yuksekgonul  
 296 et al., 2023; Oikarinen et al., 2023), and Srivastava et al. (2024) also showed that sparsity is in-  
 297 versely correlated with information leakage. They demonstrated that a dense linear classifier built  
 298 on top of a random (i.e., untrained) CBL can recover black-box accuracy if the number of concepts  
 299  $K$  approaches or exceeds the backbone feature dimension  $n$ , but this effect decreases with higher  
 300 sparsity. Related studies (Shang et al., 2024; Yan et al., 2023) similarly report that when the concept  
 301 set is large enough (e.g.,  $K \gtrsim n/2$ ), dense linear classifier can preserve black-box accuracy by re-  
 302 estimating the backbone activations therefore even using random words as concepts can match the  
 303 accuracy obtained with concepts defined by LLMs or humans.  
 304

305 While high sparsity improves interpretability and limits leakage, it naturally tends to correlate with  
 306 lower accuracy (Wong et al., 2021; Oikarinen et al., 2023; Srivastava et al., 2024), making CBM  
 307 comparison incomplete if only accuracy is reported. To address this, Srivastava et al. (2024) in-  
 308 troduced an evaluation metric named NEC, which is defined as the average number (per-class) of  
 309 non-zeros in the weights  $\mathbf{W}_F$  of the final layer  $f$ . They train  $f$  at different regularization strengths  
 310  $\lambda_{\text{CLF}}$  and accuracies are compared at equal NEC. This is convenient for enabling a fair comparison  
 311 between CBMs, but it also has limitations. Controlling NEC forces concise decision explanations,  
 312 but it does so by linearly restricting the effective concept vocabulary as the number of classes de-  
 313 creases. For instance, with three classes, NEC=5 forces  $K \leq 15$  (or even  $K = 5$  if classification  
 314 is binary) after training so that on average predictions are explained by  $\sim 5$  concepts. However, in  
 315 datasets with substantial intra-class diversity (e.g., peeled or in-field pineapples are the same class in  
 316 ImageNet), a single class may require a rich concept vocabulary (i.e., larger  $K$ ) to cover its different  
 317 contexts, even though only a subset of them is needed to predict an individual image.  
 318

319 With this in mind, we introduce a generalization of NEC, named Number of Contributing Concepts  
 320 (NCC), which does not impose a hard cap on  $K$  but still enforces concise explanations by measuring  
 321 sparsity at decision-level using concept contributions rather than weights count. To measure the con-  
 322 tribution of concept  $k$ , for class  $r$  and image  $i$ , we must consider the magnitude of both the concept  
 323 logit  $g(\mathbf{a}^{(i)})_k$  and its weight  $[\mathbf{W}_F]_{k,r}$  towards class  $r$ . We then define the absolute contribution of  
 324 a concept to a class as  $u_{k,r}^{(i)} = |[g(\mathbf{a}^{(i)})_k \cdot [\mathbf{W}_F]_{k,r}]|$ . Ideally, we want the model to recognize a  
 325 class with only a small subset of concepts that cover the vast majority of the total absolute contribu-  
 326 tion, or, in other words, explain the vast majority of the decision. Let  $u_{(s),r}^{(i)}$  denote the  $s$ -th largest  
 327

absolute contributing concept, and fixed coverage level  $\tau \in [0, 1]$ . We define NCC as:

$$\text{NCC}_\tau = \frac{1}{|\mathbb{D}|C} \sum_{i=1}^{|\mathbb{D}|} \sum_{r=1}^C \min \left\{ \kappa \in \{0, \dots, K\} : \sum_{s=1}^{\kappa} u_{(s),r}^{(i)} \geq \tau \sum_{k=1}^K u_{k,r}^{(i)} \right\}$$

Intuitively,  $\text{NCC}_\tau$  is the average number of concepts required to explain at least a  $\tau$  fraction of the prediction of a class. For example, an  $\text{NCC}=5$  with  $\tau = 0.95$ , means that, on average, just 5 concepts explain  $\geq 95\%$  of the decision. For controlling NCC, we fix a  $\tau$  and follow the approach of Srivastava et al. (2024), training  $f$  at different  $\lambda_{\text{CLF}}$  and compare CBM accuracies at equal NCC levels. In practice, targeting a lower NCC generally means trading accuracy for explanation conciseness and vice versa.

## 5 EXPERIMENTAL SETUP

**Baselines.** We compare M-CBM with three state-of-the-art CBMs: LF-CBM (Oikarinen et al., 2023), VLG-CBM (Srivastava et al., 2024), and DN-CBM (Rao et al., 2024). For VLG-CBM, we compare with a class-agnostic annotation variant, which we refer to as  $\text{VLG-CBM}_{\text{CA}}$ , rather than the original pipeline. In the original VLG-CBM, concepts are assigned to classes *before* annotation and are annotated only on images of their assigned classes. While this design reduces annotation cost, coupling concepts to classes can introduce substantial information leakage. We verify this on CUB in Figure 2. Using random words as concepts, VLG-CBM reaches black-box level accuracy already at around  $\text{NCC}=1.5$ , showing that in this setup, performance is insensitive to both sparsity and concept semantics. Intuitively, this happens because learning a concept that is labeled as positive only on images of a class is nearly equivalent to learning that class directly. When we remove class conditioning by annotating each concept across all images ( $\text{VLG-CBM}_{\text{CA}}$ ), accuracy drops substantially for both random and real concepts, and the expected interpretability–accuracy trade-off reappears. We performed the same experiment with our M-CBM, and the performance of substituting concepts with random words is similar to using random words in  $\text{VLG-CBM}_{\text{CA}}$ . However, when real concepts are used, our M-CBM outperforms  $\text{VLG-CBM}_{\text{CA}}$  at high sparsity ( $\text{NCC}=3$  to 5), while for low sparsity ( $\text{NCC}=10+$ ), accuracy becomes similar to random due to information leakage. Further implementation details for this experiment are provided in Appendix C.

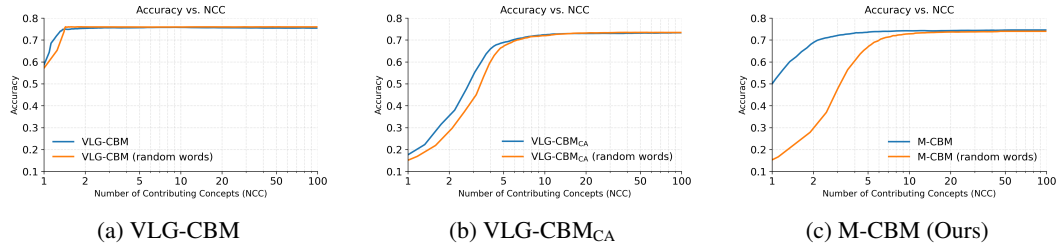


Figure 2: Accuracy vs. NCC ( $\tau = 0.95$ ) on CUB. (a) With class-conditioned annotation, VLG-CBM reaches near black-box accuracy with  $\text{NCC}=1.5$  (i.e., using only 1 to 2 concepts per prediction). The same happens using random concept names, showing evidence of leakage. (b) Making annotation class-agnostic ( $\text{VLG-CBM}_{\text{CA}}$ ) restores the accuracy–interpretability trade-off, with real concepts slightly beating random words at low NCC. (c) M-CBM outperforms both  $\text{VLG-CBM}_{\text{CA}}$  and the random baselines at low NCC, while leakage comes back in both methods as NCC increases.

**Setup.** We evaluate on three standard image classification datasets that vary in domain and class count: CUB (Wah et al., 2011), ISIC2018 (Codella et al., 2019; Tschandl et al., 2018), and ImageNet (Deng et al., 2009). CUB contains  $\sim 6k$  training images and  $\sim 5.8k$  test images of 200 fine-grained bird species. As backbone for this dataset, we use the pre-trained ResNet18 from *pytorchcv*. ISIC2018 contains dermatoscopic images of pigmented lesions categorized in 7 classes, split into  $\sim 10k$  train, 193 validation, and  $\sim 1.5k$  test. Given a pronounced class imbalance, we report both accuracy and balanced accuracy for this dataset. Given the lack of public pre-trained models, we train a ResNet50 (weighting each class by its imbalance ratio) and use it as a backbone. ImageNet includes 1k classes with  $\sim 1.3M$  training and 50k test images for general image classification. As backbone, we use the pre-trained ResNet50 from *torchvision*. Furthermore, for ImageNet

378 and CUB, we extract 10% from the train and use it as a validation set. Regarding DN-CBM, since it  
 379 only supports a CLIP backbone, we evaluate it using both the ResNet50 and ViT-B/16 backbone. As  
 380 discussed in Section 4, we compare under the same NCC. We use  $\tau = 0.95$  and measure accuracies  
 381 at NCC=5 and NCC=avg, with the latter being the average of the levels: 5, 10, 15, 20, 25, 30.  
 382

383 **Compute Resources.** We trained all neural components (SAE, CBL, and GLM-SAGA) on an  
 384 HPC cluster using an NVIDIA H200 on a multi-core node (32 cores and 512GB of RAM). On CUB  
 385 and ISIC2018, each stage takes 5-20 minutes, while 3-5 hours for ImageNet. The dominant step  
 386 in terms of cost and runtime is the annotation with GPT-4.1 API, which takes around 2 minutes  
 387 and costs USD 0.14 per concept. Concept naming was lighter, taking around 10-20 seconds and  
 388 USD 0.02 per concept, while concept merging costs were negligible. These costs scale linearly with  
 389 the concept number, which was 278, 73 and 2648 respectively for CUB, ISIC2018 and ImageNet.  
 390

## 391 6 RESULTS AND DISCUSSION

393 **Accuracy Comparison.** We report results in Table 1. Our M-CBM consistently achieves the highest  
 394 accuracy across datasets and NCC values. An expected interpretability-accuracy trade-off is also  
 395 visible across all methods, as accuracy always increases when NCC is higher (i.e., explanations are  
 396 less concise). DN-CBM consistently performs poorly, especially at NCC=5, indicating that a small  
 397 subset of generic CLIP concepts may be insufficient to predict a class across datasets. VLG-CBM<sub>CA</sub>  
 398 shows better accuracy than LF-CBM and DN-CBM, but annotating per-concept the entire dataset  
 399 with GroundingDINO makes it computationally prohibitive at ImageNet scale ( $\sim 300$  GPU-days).  
 400 In contrast, M-CBM uses SAE activations to pre-select candidate images per concept, so that we  
 401 only need to annotate  $\sim 1k$  images per concept. We exclude class-conditioned VLG-CBM from the  
 402 comparison, as due to leakage, it is effectively a black-box (see Section 5).  
 403

404 Table 1: Accuracy comparison at NCC=5 and NCC=avg with best model in bold. The results for  
 405 M-CBM are averaged over 3 seeds with same annotations. N/A denotes computationally unfeasible.

Dataset	CUB		ISIC2018				ImageNet	
	Metrics		Accuracy		Balanced Accuracy		Accuracy	
Black-box	76.67%		79.37%		75.37%		76.15%	
Sparsity	NCC=5	NCC=avg	NCC=5	NCC=avg	NCC=5	NCC=avg	NCC=5	NCC=avg
LF-CBM	58.08%	71.09%	61.44%	67.55%	64.29%	67.30%	62.20%	69.08%
DN-CBM <sub>RN</sub>	38.21%	48.98%	35.38%	54.61%	39.85%	52.85%	46.71%	57.24%
DN-CBM <sub>ViT</sub>	48.12%	66.19%	43.92%	56.08%	42.47%	53.56%	60.23%	69.98%
VLG-CBM <sub>CA</sub>	69.12%	72.25%	64.55%	72.61%	64.63%	70.80%	N/A	N/A
<b>M-CBM</b>	<b>73.70%</b>	<b>74.18%</b>	<b>72.75%</b>	<b>75.51%</b>	<b>70.14%</b>	<b>71.54%</b>	<b>72.18%</b>	<b>73.64%</b>
<b>(Ours)</b>	$\pm 0.13\%$	$\pm 0.06\%$	$\pm 0.10\%$	$\pm 0.08\%$	$\pm 0.09\%$	$\pm 0.05\%$	$\pm 0.21\%$	$\pm 0.15\%$

417 **Evaluating Concept Prediction.** We assess how well each method can learn its own concepts by  
 418 also annotating the test set. Because these labels are not ground truth, high scores do not guarantee  
 419 that the model is learning the concepts as intended, but only that they are at least internally consistent  
 420 and learnable. Especially for ISIC2018, we found that LLM-generated concept sets are often  
 421 non-visual (e.g., “warm to the touch”) or not in the data (e.g., “medical report”). Since M-CBM uses  
 422 concepts extracted from the backbone, we expect some benefits in the concept predictions, which is  
 423 what we see in Table 2. Another factor that could contribute to the lower performance is the capability  
 424 of GroundingDINO to annotate correctly, which may be inferior to asking GPT-4.1, especially  
 425 for medical images. However, due to a lack of ground truth, this remains challenging to quantify.  
 426

427 **Explanations.** We illustrate the behavior of M-CBMs through global (class-level) and local  
 428 (instance-level) explanations, using models at NCC=5. Using the final layer weights  $W_F$ , we can  
 429 visualize how concepts globally contribute to classes. In Figure 3, we show these weights using  
 430 Sankey diagrams, with “NOT concept” indicating a negative weight. For clarity, we include only  
 431 concepts with  $|W_F| > 0.1$ . On ImageNet, the model’s behavior aligns with intuition. The classes  
 “Modem” and “Radio” share concepts related to ports/switches and antennas, while they are mainly

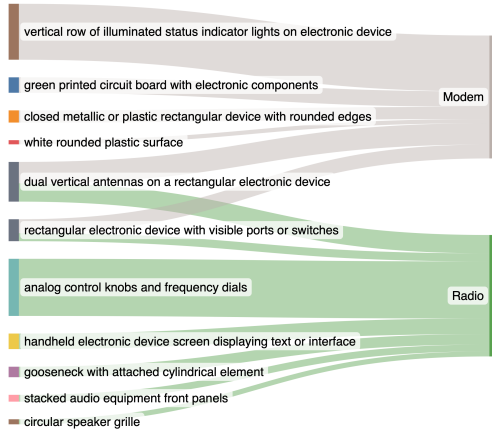
432 Table 2: ROC-AUC evaluation of concept predictions on test set. Each method is evaluated on its  
 433 own concepts. We report the macro-average across concepts and the average of the worst 10%.

434

435 Dataset	436 CUB		437 ISIC2018		438 ImageNet	
	439 Metrics		440 ROC-AUC		441 ROC-AUC	
	442 Macro	443 Worst-10%	444 Macro	445 Worst-10%	446 Macro	447 Worst-10%
448 VLG-CBM <sub>CA</sub>	449 62.03%	450 45.60%	451 73.37%	452 52.92%	453 N/A	454 N/A
455 <b>M-CBM (Ours)</b>	<b>456 90.04%</b>	<b>457 79.05%</b>	<b>458 80.57%</b>	<b>459 66.98%</b>	<b>460 88.90%</b>	<b>461 78.36%</b>

442

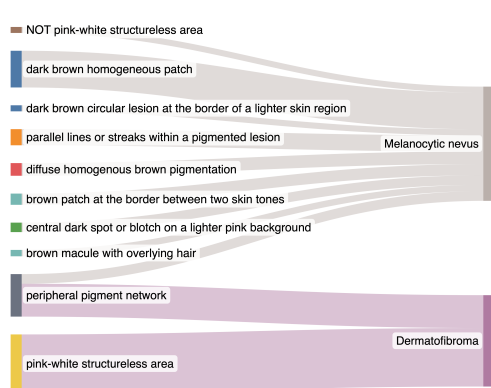
443



450

451

(a) ImageNet



(b) ISIC 2018

452

453

454 Figure 3: Sankey plots of concept–class weights of our M-CBM at NCC=5. Concepts on the left  
 455 and classes on the right. Concepts with negative weights are labeled as “NOT concept”.

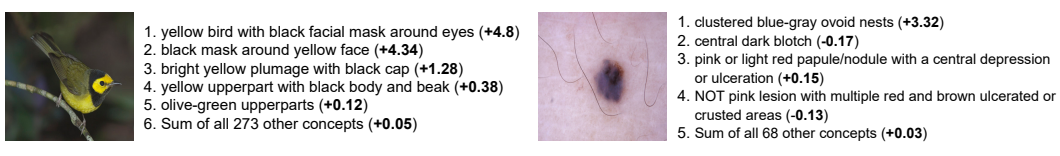
456

457

458 differentiated by the presence of indicator lights for class “Modem” versus control knobs for class  
 459 “Radio”. On ISIC2018, the model learns a richer concept set for “Melanocytic nevus” than for  
 460 “Dermatofibroma”, which could be explained by the large class imbalance. Still, the few concepts  
 461 learned for “Dermatofibroma” are consistent with dermatological literature (Zaballos et al., 2006).  
 462 Some minor concepts for “Melanocytic nevus”, such as skin-tone-related terms, are less clear. This  
 463 likely arises from the concept naming (step ②), where visually highlighting the concept (in this case,  
 464 the skin around the nevus) in the image can introduce mild artifacts that GPT-4.1 over-interpreted.  
 465 CBMs can also explain individual predictions by showing, for an input  $x^{(i)}$ , the contribution of con-  
 466 cepts to a class  $r$ . This contribution is computed directly by multiplying the logit of the  $k$ -th concept  
 467  $g(\mathbf{a}^{(i)})_k$  with its corresponding weight  $[\mathbf{W}_F]_{k,r}$  towards class  $r$ . Concepts with a negative logit are  
 468 indicated as “NOT concept”. We show two examples in Figure 4, including a correct CUB prediction  
 469 and a misclassification on ISIC, where the model incorrectly sees “clustered blue-gray ovoid  
 470 nests”, leading to a “Basal Cell Carcinoma” prediction. Zeroing this concept flips the decision to the  
 471 correct class. In both cases, we see that the decision is largely explained by the top 4-5 concepts.  
 472

473

475



476

477

478

479

480

481

482

483

484

485

486 Figure 4: Per-image explanations of M-CBM at NCC=5 for a correct prediction in CUB (a) and a  
 487 misclassification in ISIC 2018 (b). Concepts with negative logit are labeled as “NOT concept”.

## 486 7 CONCLUSION AND LIMITATIONS

488 We presented Mechanistic CBMs (M-CBM), a novel paradigm for training CBMs using concepts  
 489 learned directly from a black-box backbone and automatically annotated by an MLLM. With this  
 490 approach, we substantially improve over the state-of-the-art, both in terms of task accuracy and con-  
 491 cept predictions. We are also able to keep explanations concise by controlling final layer sparsity  
 492 to achieve a target Number of Contributing Concepts (NCC). One limitation general to all CBMs is  
 493 that we still lack a systematic way to assess whether concepts are learned as intended and not via  
 494 spurious correlations. This is because the final layer is interpretable, but the concept prediction re-  
 495 mains a black-box. Another limitation is that, while NCC allows us to control the accuracy–leakage  
 496 trade-off, it is still not enough to completely eliminate leakage, as CBMs trained on random words  
 497 still achieve higher accuracy than we would expect from random chance. Finally, compared to base-  
 498 lines, M-CBM is less plug-and-play, requiring some supervision at the SAE stage to ensure good  
 499 reconstruction and that the extracted concepts are interpretable (see Appendix B). Despite limita-  
 500 tions, given that, due to computational constraints, we annotate only a small subset of images, there  
 501 might be great potential for improvement with the advancements of MLLMs in both performance  
 502 and efficiency.

## 503 REFERENCES

505 Leonard Bereska and Stratis Gavves. Mechanistic interpretability for AI safety - a review. *Transac-*  
 506 *tions on Machine Learning Research*, 2024. ISSN 2835-8856. URL <https://openreview.net/forum?id=ePUVetPKu6>. Survey Certification, Expert Certification.

508 Steven Bills, Nick Cammarata, Dan Mossing, Henk Tillman, Leo Gao, Gabriel Goh, Ilya  
 509 Sutskever, Jan Leike, Jeff Wu, and William Saunders. Language models can explain  
 510 neurons in language models. <https://openaipublic.blob.core.windows.net/neuron-explainer/paper/index.html>, 2023.

512 Trenton Bricken, Adly Templeton, Ben Chen, Jack Lindsey, Adam Jermyn, Shan Carter, Tom  
 513 Henighan, Adam Pearce, and Chris Olah. Towards monosemanticity: Decomposing lan-  
 514 guage models with dictionary learning. <https://transformer-circuits.pub/2023/monosemantic-features>, 2023. Transformer Circuits Thread, Anthropic.

516 Noel Codella, Veronica Rotemberg, Philipp Tschandl, M. Emre Celebi, Stephen Dusza, David Gut-  
 517 man, Brian Helba, Aadi Kalloo, Konstantinos Liopyris, Michael Marchetti, Harald Kittler, and  
 518 Allan Halpern. Skin lesion analysis toward melanoma detection 2018: A challenge hosted by  
 519 the international skin imaging collaboration (isic), 2019. URL <https://arxiv.org/abs/1902.03368>.

522 Arthur Conmy, Augustine N. Mavor-Parker, Aengus Lynch, Stefan Heimersheim, and Adrià  
 523 Garriga-Alonso. Towards automated circuit discovery for mechanistic interpretability. In  
 524 *Thirty-seventh Conference on Neural Information Processing Systems*, 2023. URL <https://openreview.net/forum?id=89ia77nZ8u>.

526 Antonio De Santis, Riccardo Campi, Matteo Bianchi, and Marco Brambilla. Visual-tcav: Concept-  
 527 based attribution and saliency maps for post-hoc explainability in image classification, 2025. URL  
 528 <https://arxiv.org/abs/2411.05698>.

532 Jia Deng, Wei Dong, Richard Socher, Li-Jia Li, Kai Li, and Li Fei-Fei. Imagenet: A large-scale hier-  
 533 archical image database. In *2009 IEEE Conference on Computer Vision and Pattern Recognition*,  
 534 pp. 248–255, 2009. doi: 10.1109/CVPR.2009.5206848.

536 Nelson Elhage, Tristan Hume, Catherine Olsson, Nicholas Schiefer, Tom Henighan, Shauna Kravec,  
 537 Zac Hatfield-Dodds, Robert Lasenby, Dawn Drain, Carol Chen, Roger Grosse, Sam McCandlish,  
 538 Jared Kaplan, Dario Amodei, Martin Wattenberg, and Christopher Olah. Toy models of superpo-  
 539 sition, 2022. URL <https://arxiv.org/abs/2209.10652>.

542 Thomas Fel, Agustin Picard, Louis Béthune, Thibaut Boissin, David Vigouroux, Julien Colin, Rémi  
 543 Cadène, and Thomas Serre. Craft: Concept recursive activation factorization for explainability. In  
 544 *Proceedings of the IEEE/CVF Conference on Computer Vision and Pattern Recognition (CVPR)*,  
 545 pp. 2711–2721, June 2023.

540 Leo Gao, Tom Dupre la Tour, Henk Tillman, Gabriel Goh, Rajan Troll, Alec Radford, Ilya Sutskever,  
 541 Jan Leike, and Jeffrey Wu. Scaling and evaluating sparse autoencoders. In *The Thirteenth Inter-*  
 542 *national Conference on Learning Representations*, 2025. URL [https://openreview.net/](https://openreview.net/forum?id=tcsZt9ZNKD)  
 543 [forum?id=tcsZt9ZNKD](https://openreview.net/forum?id=tcsZt9ZNKD).

544 Amirata Ghorbani, James Wexler, James Y Zou, and Been Kim. Towards automatic concept-based  
 545 explanations. In H. Wallach, H. Larochelle, A. Beygelzimer, F. d'Alché-Buc, E. Fox, and R. Gar-  
 546 nett (eds.), *Advances in Neural Information Processing Systems*, volume 32. Curran Associates,  
 547 Inc., 2019.

548 Liv Gorton. The missing curve detectors of inceptionv1: Applying sparse autoencoders to in-  
 549 ceptionv1 early vision. In *ICML 2024 Workshop on Mechanistic Interpretability*, 2024. URL  
 550 <https://openreview.net/forum?id=IGnoozsfj1>.

552 Marton Havasi, Sonali Parbhoo, and Finale Doshi-Velez. Addressing leakage in concept bottleneck  
 553 models. In S. Koyejo, S. Mohamed, A. Agarwal, D. Belgrave, K. Cho, and A. Oh (eds.), *Advances*  
 554 *in Neural Information Processing Systems*, volume 35, pp. 23386–23397. Curran Associates, Inc.,  
 555 2022a. URL [https://proceedings.neurips.cc/paper\\_files/paper/2022/](https://proceedings.neurips.cc/paper_files/paper/2022/file/944ecf65a46feb578a43abfd5cddd960-Paper-Conference.pdf)  
 556 [file/944ecf65a46feb578a43abfd5cddd960-Paper-Conference.pdf](https://proceedings.neurips.cc/paper_files/paper/2022/file/944ecf65a46feb578a43abfd5cddd960-Paper-Conference.pdf).

557 Marton Havasi, Sonali Parbhoo, and Finale Doshi-Velez. Addressing leakage in concept bottleneck  
 558 models. In *Proceedings of the 36th International Conference on Neural Information Processing*  
 559 *Systems*, NIPS '22, Red Hook, NY, USA, 2022b. Curran Associates Inc. ISBN 9781713871088.

560 Robert Huben, Hoagy Cunningham, Logan Riggs Smith, Aidan Ewart, and Lee Sharkey. Sparse  
 561 autoencoders find highly interpretable features in language models. In *The Twelfth International*  
 562 *Conference on Learning Representations*, 2024. URL [https://openreview.net/](https://openreview.net/forum?id=F76bwRSLeK)  
 563 [forum?id=F76bwRSLeK](https://openreview.net/forum?id=F76bwRSLeK).

564 Been Kim, Martin Wattenberg, Justin Gilmer, Carrie Cai, James Wexler, Fernanda Viegas, and Rory  
 565 sayres. Interpretability beyond feature attribution: Quantitative testing with concept activation  
 566 vectors (TCAV). In Jennifer Dy and Andreas Krause (eds.), *Proceedings of the 35th International*  
 567 *Conference on Machine Learning*, volume 80 of *Proceedings of Machine Learning Research*, pp.  
 568 2668–2677. PMLR, 10–15 Jul 2018. URL [https://proceedings.mlr.press/v80/](https://proceedings.mlr.press/v80/kim18d.html)  
 569 [kim18d.html](https://proceedings.mlr.press/v80/kim18d.html).

570 Pang Wei Koh, Thao Nguyen, Yew Siang Tang, Stephen Mussmann, Emma Pierson, Been Kim, and  
 571 Percy Liang. Concept bottleneck models. In Hal Daumé III and Aarti Singh (eds.), *Proceedings of*  
 572 *the 37th International Conference on Machine Learning*, volume 119 of *Proceedings of Machine*  
 573 *Learning Research*, pp. 5338–5348. PMLR, 13–18 Jul 2020. URL [https://proceedings.](https://proceedings.mlr.press/v119/koh20a.html)  
 574 [mlr.press/v119/koh20a.html](https://proceedings.mlr.press/v119/koh20a.html).

575 Shilong Liu, Zhaoyang Zeng, Tianhe Ren, Feng Li, Hao Zhang, Jie Yang, Qing Jiang, Chunyuan Li,  
 576 Jianwei Yang, Hang Su, Jun Zhu, and Lei Zhang. Grounding dino: Marrying dino with grounded  
 577 pre-training for open-set object detection. In Aleš Leonardis, Elisa Ricci, Stefan Roth, Olga  
 578 Russakovsky, Torsten Sattler, and Gü̈l Varol (eds.), *Computer Vision – ECCV 2024*, pp. 38–55,  
 579 Cham, 2025. Springer Nature Switzerland. ISBN 978-3-031-72970-6.

580 Tuomas Oikarinen and Tsui-Wei Weng. Clip-dissect: Automatic description of neuron representa-  
 581 tions in deep vision networks. *International Conference on Learning Representations*, 2023.

582 Tuomas Oikarinen, Subhro Das, Lam M. Nguyen, and Tsui-Wei Weng. Label-free concept bottle-  
 583 neck models. In *The Eleventh International Conference on Learning Representations*, 2023. URL  
 584 [https://openreview.net/](https://openreview.net/forum?id=F1Cg47MNvBA)  
 585 [forum?id=F1Cg47MNvBA](https://openreview.net/forum?id=F1Cg47MNvBA).

586 Chris Olah, Nick Cammarata, Ludwig Schubert, Gabriel Goh, Michael Petrov, and Shan Carter.  
 587 Zoom in: An introduction to circuits. *Distill*, 2020. doi: 10.23915/distill.00024.001.  
 588 <https://distill.pub/2020/circuits/zoom-in>.

589 Alec Radford, Jong Wook Kim, Chris Hallacy, Aditya Ramesh, Gabriel Goh, Sandhini Agar-  
 590 wal, Girish Sastry, Amanda Askell, Pamela Mishkin, Jack Clark, Gretchen Krueger, and Ilya  
 591 Sutskever. Learning transferable visual models from natural language supervision. In Marina

592 <https://distill.pub/2020/circuits/zoom-in>.

593

594 Meila and Tong Zhang (eds.), *Proceedings of the 38th International Conference on Machine*  
 595 *Learning*, volume 139 of *Proceedings of Machine Learning Research*, pp. 8748–8763. PMLR,  
 596 18–24 Jul 2021. URL <https://proceedings.mlr.press/v139/radford21a.html>.

597

598 Senthooran Rajamanoharan, Arthur Conmy, Lewis Smith, Tom Lieberum, Vikrant Varma,  
 599 János Kramár, Rohin Shah, and Neel Nanda. Improving sparse decomposition of lan-  
 600 guage model activations with gated sparse autoencoders. In A. Globerson, L. Mackey,  
 601 D. Belgrave, A. Fan, U. Paquet, J. Tomczak, and C. Zhang (eds.), *Advances in Neu-  
 602 ral Information Processing Systems*, volume 37, pp. 775–818. Curran Associates, Inc.,  
 603 2024. URL [https://proceedings.neurips.cc/paper\\_files/paper/2024/file/01772a8b0420baec00c4d59fe2fbace6-Paper-Conference.pdf](https://proceedings.neurips.cc/paper_files/paper/2024/file/01772a8b0420baec00c4d59fe2fbace6-Paper-Conference.pdf).

604

605 Sukrut Rao, Sweta Mahajan, Moritz Böhle, and Bernt Schiele. Discover-then-name: Task-agnostic  
 606 concept bottlenecks via automated concept discovery. In *European Conference on Computer*  
 607 *Vision*, 2024.

608

609 Karsten Roth, Jae Myung Kim, A. Sophia Koepke, Oriol Vinyals, Cordelia Schmid, and Zeynep  
 610 Akata. Waffling around for performance: Visual classification with random words and broad  
 611 concepts. In *2023 IEEE/CVF International Conference on Computer Vision (ICCV)*, pp. 15700–  
 612 15711, 2023. doi: 10.1109/ICCV51070.2023.01443.

613

614 Tamar Rott Shaham, Sarah Schwettmann, Franklin Wang, Achyuta Rajaram, Evan Hernandez, Jacob  
 615 Andreas, and Antonio Torralba. A multimodal automated interpretability agent. In *Forty-first*  
*616 International Conference on Machine Learning*, 2024.

617

618 Lisa Schut, Nenad Tomašev, Thomas McGrath, Demis Hassabis, Ulrich Paquet, and Been  
 619 Kim. Bridging the human–ai knowledge gap through concept discovery and transfer in alp-  
 620 hazero. *Proceedings of the National Academy of Sciences*, 122(13):e2406675122, 2025. doi:  
 621 10.1073/pnas.2406675122. URL <https://www.pnas.org/doi/abs/10.1073/pnas.2406675122>.

622

623 Ramprasaath R. Selvaraju, Michael Cogswell, Abhishek Das, Ramakrishna Vedantam, Devi Parikh,  
 624 and Dhruv Batra. Grad-cam: Visual explanations from deep networks via gradient-based localiza-  
 625 tion. In *2017 IEEE International Conference on Computer Vision (ICCV)*. IEEE, October 2017.  
 doi: 10.1109/iccv.2017.74. URL <http://dx.doi.org/10.1109/ICCV.2017.74>.

626

627 Chenming Shang, Shiji Zhou, Hengyuan Zhang, Xinzhe Ni, Yujiu Yang, and Yuwang Wang. In-  
 628 cremental Residual Concept Bottleneck Models . In *2024 IEEE/CVF Conference on Com-  
 629 puter Vision and Pattern Recognition (CVPR)*, pp. 11030–11040, Los Alamitos, CA, USA,  
 630 June 2024. IEEE Computer Society. doi: 10.1109/CVPR52733.2024.01049. URL <https://doi.ieeecomputersociety.org/10.1109/CVPR52733.2024.01049>.

631

632 David Silver, Thomas Hubert, Julian Schrittwieser, Ioannis Antonoglou, Matthew Lai, Arthur Guez,  
 633 Marc Lanctot, Laurent Sifre, Dharsan Kumaran, Thore Graepel, Timothy Lillicrap, Karen Si-  
 634 monyan, and Demis Hassabis. Mastering chess and shogi by self-play with a general reinforce-  
 635 ment learning algorithm, 2017. URL <https://arxiv.org/abs/1712.01815>.

636

637 Robyn Speer, Joshua Chin, and Catherine Havasi. Conceptnet 5.5: An open multilingual graph  
 638 of general knowledge. *Proceedings of the AAAI Conference on Artificial Intelligence*, 31(1),  
 639 Feb. 2017. doi: 10.1609/aaai.v31i1.11164. URL <https://ojs.aaai.org/index.php/AAAI/article/view/11164>.

640

641 Divyansh Srivastava, Ge Yan, and Tsui-Wei Weng. Vlg-cbm: Training concept bottle-  
 642 neck models with vision-language guidance. In A. Globerson, L. Mackey, D. Bel-  
 643 grave, A. Fan, U. Paquet, J. Tomczak, and C. Zhang (eds.), *Advances in Neural In-  
 644 formation Processing Systems*, volume 37, pp. 79057–79094. Curran Associates, Inc.,  
 645 2024. URL [https://proceedings.neurips.cc/paper\\_files/paper/2024/file/90043ebd68500f9efe84fedf860a64f3-Paper-Conference.pdf](https://proceedings.neurips.cc/paper_files/paper/2024/file/90043ebd68500f9efe84fedf860a64f3-Paper-Conference.pdf).

646

647 Mukund Sundararajan, Ankur Taly, and Qiqi Yan. Axiomatic attribution for deep networks. In  
 648 *Proceedings of the 34th International Conference on Machine Learning - Volume 70*, ICML’17,  
 649 pp. 3319–3328. JMLR.org, 2017.

648 Harrish Thasarathan, Julian Forsyth, Thomas Fel, Matthew Kowal, and Konstantinos G. Derpanis.  
 649 Universal sparse autoencoders: Interpretable cross-model concept alignment. In *Forty-second*  
 650 *International Conference on Machine Learning*, 2025. URL [https://openreview.net/](https://openreview.net/forum?id=UoaxRN88oR)  
 651 [forum?id=UoaxRN88oR](https://openreview.net/forum?id=UoaxRN88oR).

652 Philipp Tschandl, Cliff Rosendahl, and Harald Kittler. The ham10000 dataset, a large col-  
 653 lection of multi-source dermatoscopic images of common pigmented skin lesions. *Scientific*  
 654 *Data*, 5:180161, 2018. doi: 10.1038/sdata.2018.161. URL [https://www.nature.com/](https://www.nature.com/articles/sdata2018161)  
 655 [articles/sdata2018161](https://www.nature.com/articles/sdata2018161).

656 C. Wah, S. Branson, P. Welinder, P. Perona, and S. Belongie. The caltech-ucsd birds-200-2011  
 657 dataset. Technical Report CNS-TR-2011-001, California Institute of Technology, 2011.

658 Eric Wong, Shibani Santurkar, and Aleksander Madry. Leveraging sparse linear layers for debug-  
 659 gable deep networks. In Marina Meila and Tong Zhang (eds.), *Proceedings of the 38th Inter-*  
 660 *national Conference on Machine Learning*, volume 139 of *Proceedings of Machine Learning*  
 661 *Research*, pp. 11205–11216. PMLR, 18–24 Jul 2021. URL [https://proceedings.mlr.](https://proceedings.mlr.press/v139/wong21b.html)  
 662 [press/v139/wong21b.html](https://proceedings.mlr.press/v139/wong21b.html).

663 Feiyu Xu, Hans Uszkoreit, Yangzhou Du, Wei Fan, Dongyan Zhao, and Jun Zhu. *Explainable AI: A Brief Survey on History, Research Areas, Approaches and Challenges*, pp. 563–574. 09 2019.  
 664 ISBN 978-3-030-32235-9. doi: 10.1007/978-3-030-32236-6\_51.

665 An Yan, Yu Wang, Yiwu Zhong, Chengyu Dong, Zexue He, Yujie Lu, William Yang Wang, Jingbo  
 666 Shang, and Julian McAuley. Learning Concise and Descriptive Attributes for Visual Recognition  
 667 . In *2023 IEEE/CVF International Conference on Computer Vision (ICCV)*, pp. 3067–3077, Los  
 668 Alamitos, CA, USA, October 2023. IEEE Computer Society. doi: 10.1109/ICCV51070.2023.  
 669 00287. URL [https://doi.ieee.org/10.1109/ICCV51070.](https://doi.ieee.org/10.1109/ICCV51070.2023.00287)  
 670 2023.00287.

671 Yue Yang, Artemis Panagopoulou, Shenghao Zhou, Daniel Jin, Chris Callison-Burch, and Mark  
 672 Yatskar. Language in a bottle: Language model guided concept bottlenecks for interpretable im-  
 673 age classification. In *Proceedings of the IEEE/CVF Conference on Computer Vision and Pattern*  
 674 *Recognition*, pp. 19187–19197, 2023.

675 Chih-Kuan Yeh, Been Kim, Sercan Ö. Arik, Chun-Liang Li, Tomas Pfister, and Pradeep Ravikumar.  
 676 On completeness-aware concept-based explanations in deep neural networks. In *Proceedings of*  
 677 *the 34th International Conference on Neural Information Processing Systems, NIPS '20*, Red  
 678 Hook, NY, USA, 2020. Curran Associates Inc. ISBN 9781713829546.

679 Mert Yuksekgonul, Maggie Wang, and James Zou. Post-hoc concept bottleneck models. In  
 680 *The Eleventh International Conference on Learning Representations*, 2023. URL <https://openreview.net/forum?id=nA5AZ8CEyow>.

681 P. Zaballos, Á. Llambrich, M. Ara, Z. Olazarán, J. Malvehy, and S. Puig. Dermoscopic findings of  
 682 haemosiderotic and aneurysmal dermatofibroma: report of six patients. *British Journal of Der-  
 683 matology*, 154(2):244–250, 02 2006. ISSN 0007-0963. doi: 10.1111/j.1365-2133.2005.06844.x.  
 684 URL <https://doi.org/10.1111/j.1365-2133.2005.06844.x>.

685 Mateo Espinosa Zarlenga, Pietro Barbiero, Zohreh Shams, Dmitry Kazhdan, Umang Bhatt, Adrian  
 686 Weller, and Mateja Jamnik. Towards robust metrics for concept representation evaluation. In  
 687 *Proceedings of the Thirty-Seventh AAAI Conference on Artificial Intelligence and Thirty-Fifth*  
 688 *Conference on Innovative Applications of Artificial Intelligence and Thirteenth Symposium on*  
 689 *Educational Advances in Artificial Intelligence, AAAI'23/IAAI'23/EAAI'23*. AAAI Press, 2023.  
 690 ISBN 978-1-57735-880-0. doi: 10.1609/aaai.v37i10.26392. URL [https://doi.org/10.](https://doi.org/10.1609/aaai.v37i10.26392)  
 691 [1609/aaai.v37i10.26392](https://doi.org/10.1609/aaai.v37i10.26392).

692 Rui Zhang, Xingbo Du, Junchi Yan, and Shihua Zhang. The decoupling concept bottleneck model.  
 693 *IEEE Transactions on Pattern Analysis and Machine Intelligence*, 47(2):1250–1265, 2025. doi:  
 694 10.1109/TPAMI.2024.3489597.

Ruihan Zhang, Prashan Madumal, Tim Miller, Krista A. Ehinger, and Benjamin I. P. Rubinstein. Invertible concept-based explanations for cnn models with non-negative concept activation vectors. *Proceedings of the AAAI Conference on Artificial Intelligence*, 35(13):11682–11690, May 2021. doi: 10.1609/aaai.v35i13.17389. URL <https://ojs.aaai.org/index.php/AAAI/article/view/17389>.

Hui Zou and Trevor Hastie. Regularization and variable selection via the elastic net. *Journal of the Royal Statistical Society Series B: Statistical Methodology*, 67(2):301–320, 03 2005. ISSN 1369-7412. doi: 10.1111/j.1467-9868.2005.00503.x. URL <https://doi.org/10.1111/j.1467-9868.2005.00503.x>.

## A APPENDIX OVERVIEW

In the appendix, we provide:

- B. Details on training SAEs
- C. Details on random words CBMs
- D. Summary of CBMs parameters and backbones
- E. Visualizations of CBL neurons
- F. More examples of explanations
- G. Additional experiments on dataset annotation
- H. Accuracies under NEC
- I. Visualizing SAE features
- J. Explanations compared with baselines

## B DETAILS ON TRAINING SAEs

In this section, we detail how we trained and evaluated SAEs for concept extraction. We did not find a single hyperparameter configuration that worked uniformly across datasets or backbones. Some dataset-specific adjustments were typically required. Following Bricken et al. (2023), we relied on a mix of quantitative and qualitative proxies to judge whether an SAE was “good enough” for downstream concept use. Specifically, we tracked the following metrics:

1. **L2 reconstruction loss.** We want the reconstruction loss to be low to ensure we extract a comprehensive set of concepts.
2. **Average  $\ell_0$ .** We aim for a number significantly lower than the backbone dimensionality to ensure concepts are disentangled.
3. **Feature density histograms.** It shows how many hidden neurons fire at different activation frequencies across the training set. In the ideal scenario, neurons are either dead or represent interpretable concepts, so we look for a histogram with two clusters, one with very low density representing dead or noisy features and one with higher density, which should represent the actual concepts.
4. **Recovered cross-entropy loss.** We ideally want the extracted concepts to recover model performance, so we know they have predictive power.
5. **Recovered accuracy.** Same as 4. For ISIC2018, we also consider balanced accuracy.
6. **Manual inspection.** Inspecting top-activating images for random neurons in the high-density cluster to assess whether the learned concepts seem interpretable. Empirically, we found that when all other metrics are healthy, most concepts are interpretable, although this cannot be guaranteed.

In Table 3, we provide the training hyperparameters for the SAEs used in the paper, while in Table 4, we show the results in terms of the evaluation metrics we monitored. In Figure 5, we provide the Feature Density Histograms for each SAE. We can see that low-density neurons are generally well

separated from high-density neurons. Furthermore, most of the low-density neurons are dead, i.e., never activating. Some neurons are neither dead nor high-density, and these are typically noisy and not very important for the task. As explained in Section 3, we perform a filtering step to remove these neurons before naming and annotation. In Figure 6, we show how choosing a different feature density cut-off impacts recovered loss, accuracy, and the number of neurons kept. We highlight the cut-off we used with a red star symbol. As we see, removing neurons with very low density has little impact on cross-entropy loss and accuracy. After pruning, recovered loss and accuracy for CUB become 89.40% and 98.41%. For ISIC2018, recovered loss and balanced accuracy become 99.41% and 96.84%. For ImageNet recovered loss and accuracy become 97.63% and 96.60%.

Table 3: Training hyperparameters for the SAEs used in the paper.

Hyperparameter	CUB	ISIC2018	ImageNet
Backbone layer dimension	512	2048	2048
Expansion factor	1 $\times$	0.25 $\times$	4 $\times$
Optimizer	Adam	Adam	Adam
Learning rate	$1 \times 10^{-4}$	$1 \times 10^{-4}$	$1 \times 10^{-3}$
L1 coefficient ( $\lambda_{\text{SAE}}$ )	$2 \times 10^{-3}$	$5 \times 10^{-4}$	$1 \times 10^{-3}$
Epochs	1000	1000	1000
Patience for early stopping	50	50	50

Table 4: Quantitative evaluation metrics for the SAEs we used in the concept extraction phase. These are computed on the validation set, except for  $\ell_0$ , which is computed on the training set.

Metric	CUB	ISIC2018	ImageNet
L2 reconstruction loss	0.0231	0.0066	0.0462
Average $\ell_0$	7.66	17.14	39.23
Recovered loss (CE)	89.49%	99.58	97.74%
Recovered accuracy	98.39%	acc: 96.08%, bal. acc: 96.84%	96.68%

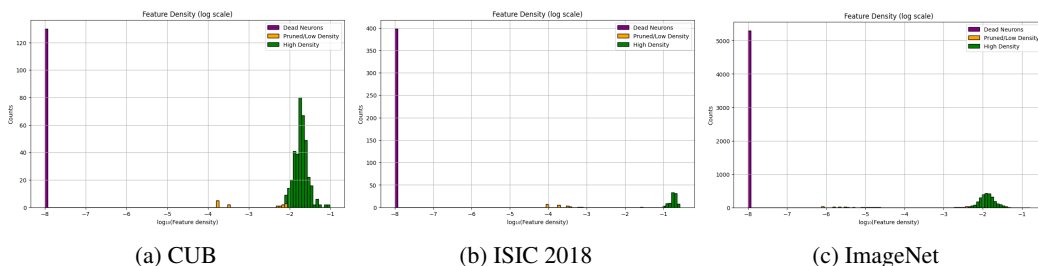


Figure 5: Feature density histogram for CUB, ISIC2018 and ImageNet. Purple indicates dead neurons (never active in the training set). Yellow indicates neurons that were pruned due to low density and little to no impact on recovered loss. Green indicates neurons that are kept as concepts for the subsequent steps.

## C DETAILS ON RANDOM WORDS CBMs

In this section, we provide additional details on how we implemented the experiments with random words for VLG-CBM, VLG-CBM<sub>CA</sub>, and M-CBM. For each method, we replace every concept name with a random, semantically meaningless text while preserving the cardinality of the original concept sets and their class-conditioned assignment for vanilla VLG-CBM. We draw words from the NLTK’s words corpus, filtered to lowercase alphabetic strings of length 3–8, and added the prefix “bird\_” so that the result is a short phrase like “bird pizza”. The prefix helps maintain minimum image relevance so that models like GroundingDINO or GPT4.1 are more likely to annotate

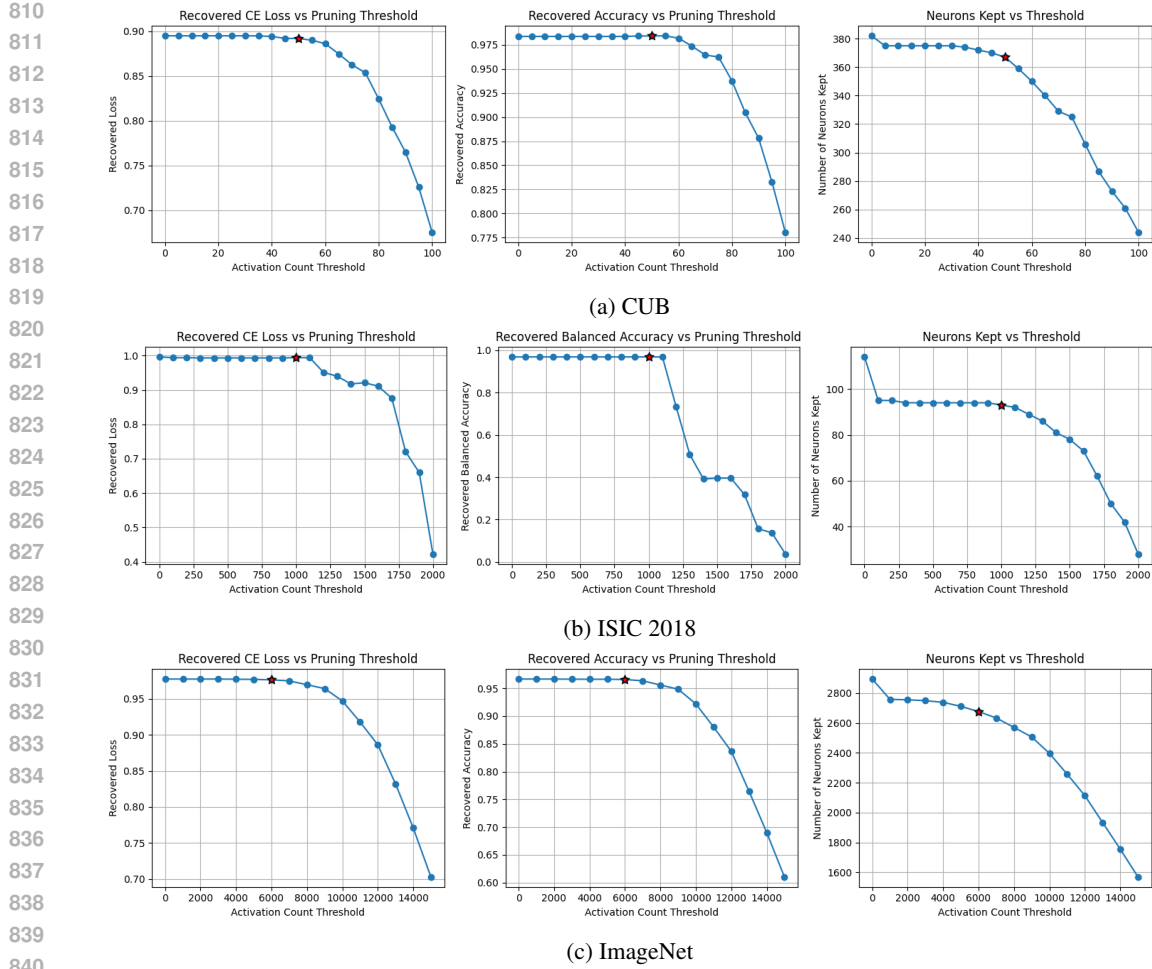


Figure 6: Effect of pruning by activation-count threshold for CUB, ISIC2018, and ImageNet. Higher thresholds typically reduce recovered performance, but when discarding low-density neurons, the reduction tends to be negligible. The point highlighted by a red star indicates the cutoff used in our experiments.

the random concepts as positive in some of the images. For VLG-CBM, the annotation is done using their official codebase without modifications, while for VLG-CBM<sub>CA</sub>, we remove class conditioning and annotate each (random) concept across all images. Because GroundingDINO accepts at most 256 input tokens, we batch concept lists and run multiple passes until all concepts are processed. For M-CBM, we follow our standard pipeline but substitute random names before annotation. Furthermore, when annotating random concepts, we omit reference grids of top-activating images to avoid leaking information about the original concepts. Figure 20 illustrates how, under class-conditioned annotation, VLG-CBM can effortlessly predict correctly using only 1–2 random concepts.

## D SUMMARY OF CBMS PARAMETERS AND BACKBONES

In this section, we report the number of parameters used at inference time for all methods and datasets. For each configuration, we decompose the total parameter count into (i) the pre-trained backbone, and (ii) the CBL plus the final classifier, which we denote as CBM. The CBL size  $K$  corresponds to the dimensionality of the concept bottleneck (i.e., the total number of concepts). It differs across methods, because each CBM constructs and filters its concept set using its own procedure. Table 5 summarizes the parameter counts (in millions) for all methods considered in our main experiments. Differences are largely dominated by the choice of backbone (e.g., CLIP ViT-

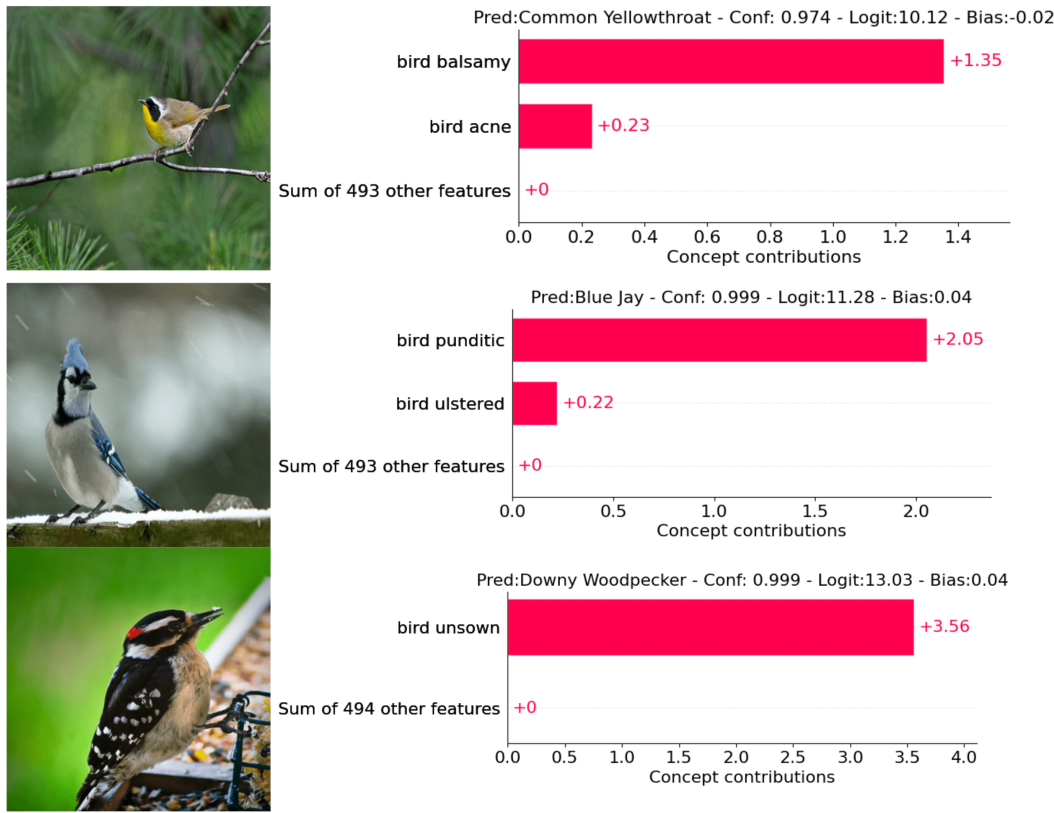


Figure 7: Examples of VLG-CBM explanations where replacing all concept names with random ones still yields correct predictions using just 1–2 concepts, illustrating how class-conditioned annotation can leak class-specific information unrelated to concept semantics.

Table 5: Inference-time parameter counts (in millions). Backbone counts include only the pretrained feature extractor. CBM counts include the CBL and the final classifier.

Method	Dataset	Backbone	Backbone (M)	CBL $K$	CBM (M)	Total (M)
LF-CBM	CUB	ResNet-18	11.69	208	0.15	11.84
LF-CBM	ISIC2018	ResNet-50	25.56	35	0.07	25.63
LF-CBM	ImageNet	ResNet-50	25.56	4523	13.79	39.35
DN-CBM <sub>RN</sub>	CUB	CLIP RN50	38.30	8192	10.04	48.34
DN-CBM <sub>RN</sub>	ISIC2018	CLIP RN50	38.30	8192	8.45	46.75
DN-CBM <sub>RN</sub>	ImageNet	CLIP RN50	38.30	8192	16.59	54.89
DN-CBM <sub>ViT</sub>	CUB	CLIP ViT-B/16	86.20	4096	2.92	89.12
DN-CBM <sub>ViT</sub>	ISIC2018	CLIP ViT-B/16	86.20	4096	2.13	88.33
DN-CBM <sub>ViT</sub>	ImageNet	CLIP ViT-B/16	86.20	4096	6.20	92.40
VLG-CBM <sub>CA</sub>	CUB	ResNet-18	11.69	535	0.38	12.07
VLG-CBM <sub>CA</sub>	ISIC2018	ResNet-50	25.56	80	0.16	25.72
VLG-CBM <sub>CA</sub>	ImageNet	–	–	N/A	N/A	N/A
<b>M-CBM (Ours)</b>	CUB	ResNet-18	<b>11.69</b>	<b>278</b>	<b>0.20</b>	<b>11.89</b>
<b>M-CBM (Ours)</b>	ISIC2018	ResNet-50	<b>25.56</b>	<b>73</b>	<b>0.15</b>	<b>25.71</b>
<b>M-CBM (Ours)</b>	ImageNet	ResNet-50	<b>25.56</b>	<b>2648</b>	<b>8.07</b>	<b>33.63</b>

B/16 vs ResNet-18/50), while the additional parameters introduced by the CBM head are relatively small in all cases.

918 E VISUALIZATIONS OF CBL NEURONS  
919920 In Figures 8, 9, and 10 we show the top-5 activating test images for representative concepts on  
921 CUB, ISIC2018, and ImageNet, respectively. These visualizations qualitatively assess whether CBL  
922 concepts align with their intended semantics and, when paired with model explanations, help convey  
923 *what* the model is actually seeing in the image that influences a prediction.  
924925 F MORE EXAMPLES OF EXPLANATIONS  
926927 In this section, we provide additional examples of local explanations of our M-CBMs at NCC=5.  
928 The explanations are shown in Figures 11, 12, and 13 respectively from the CUB, ISIC2018, and  
929 ImageNet test sets.  
930  
931  
932  
933  
934  
935  
936  
937  
938  
939  
940  
941  
942  
943  
944  
945  
946  
947  
948  
949  
950  
951  
952  
953  
954  
955  
956  
957  
958  
959  
960  
961  
962  
963  
964  
965  
966  
967  
968  
969  
970  
971



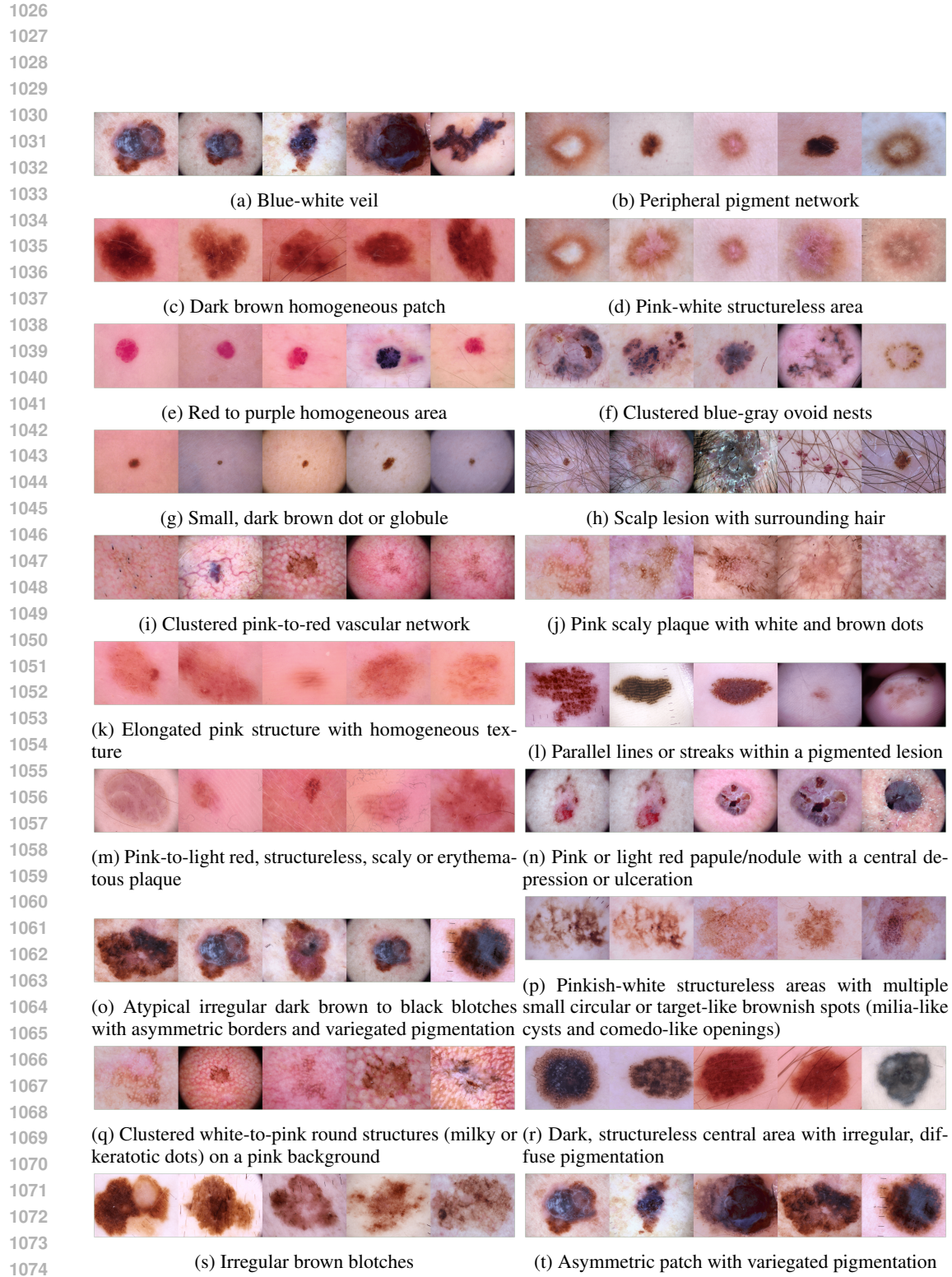


Figure 9: Top-5 activating images for ISIC2018 concepts

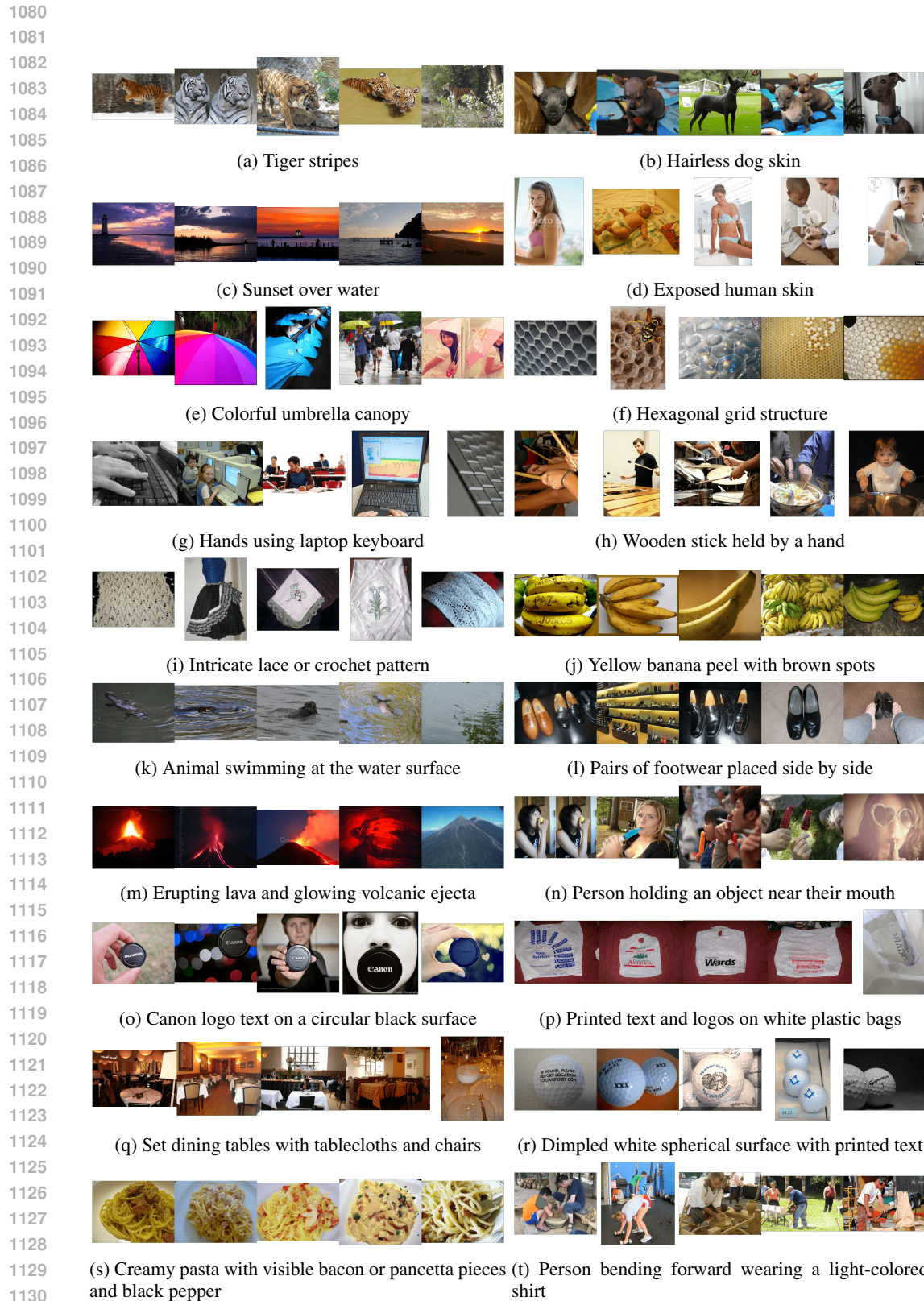


Figure 10: Top-5 activating images for ImageNet concepts

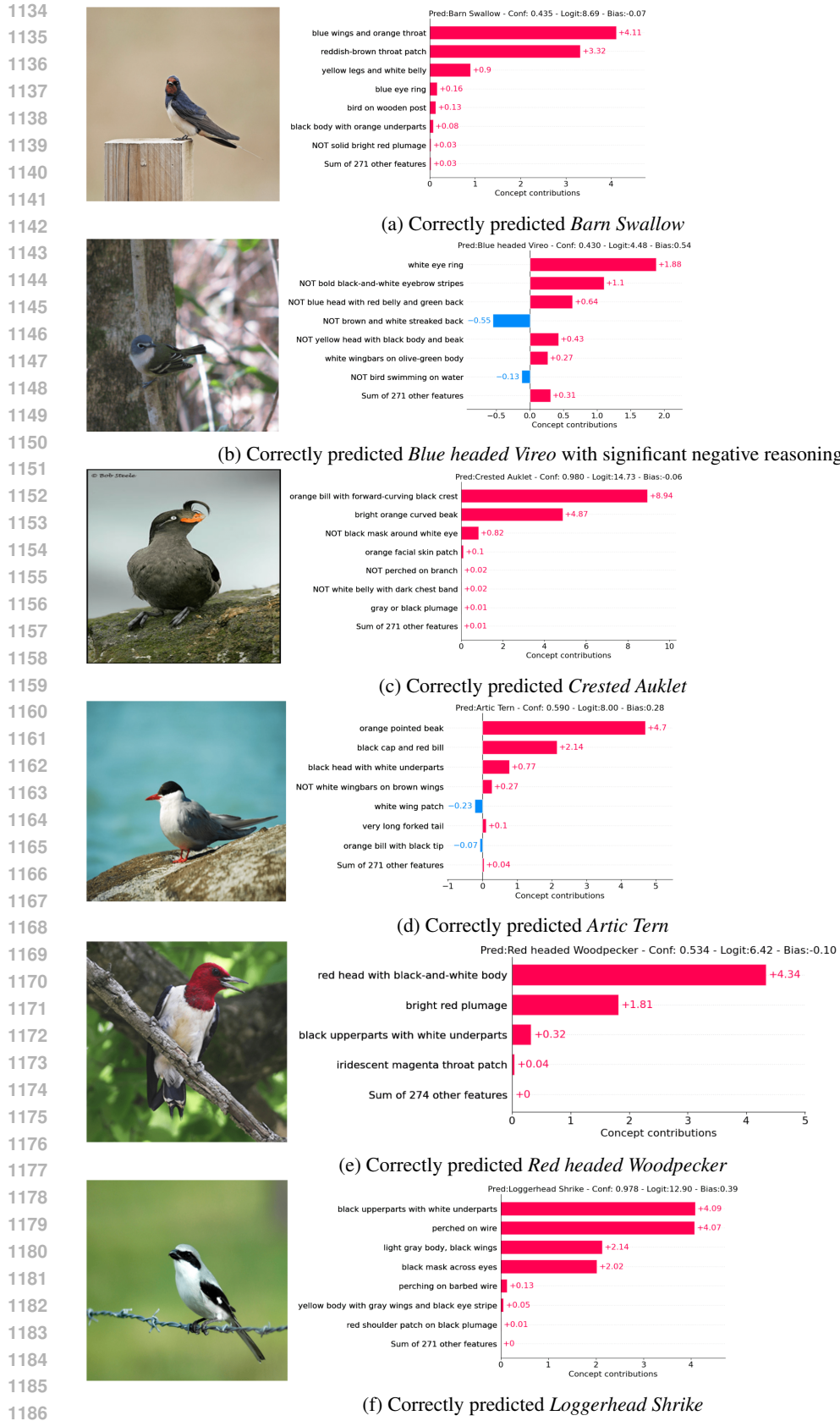


Figure 11: Examples of local explanations from CUB test set.

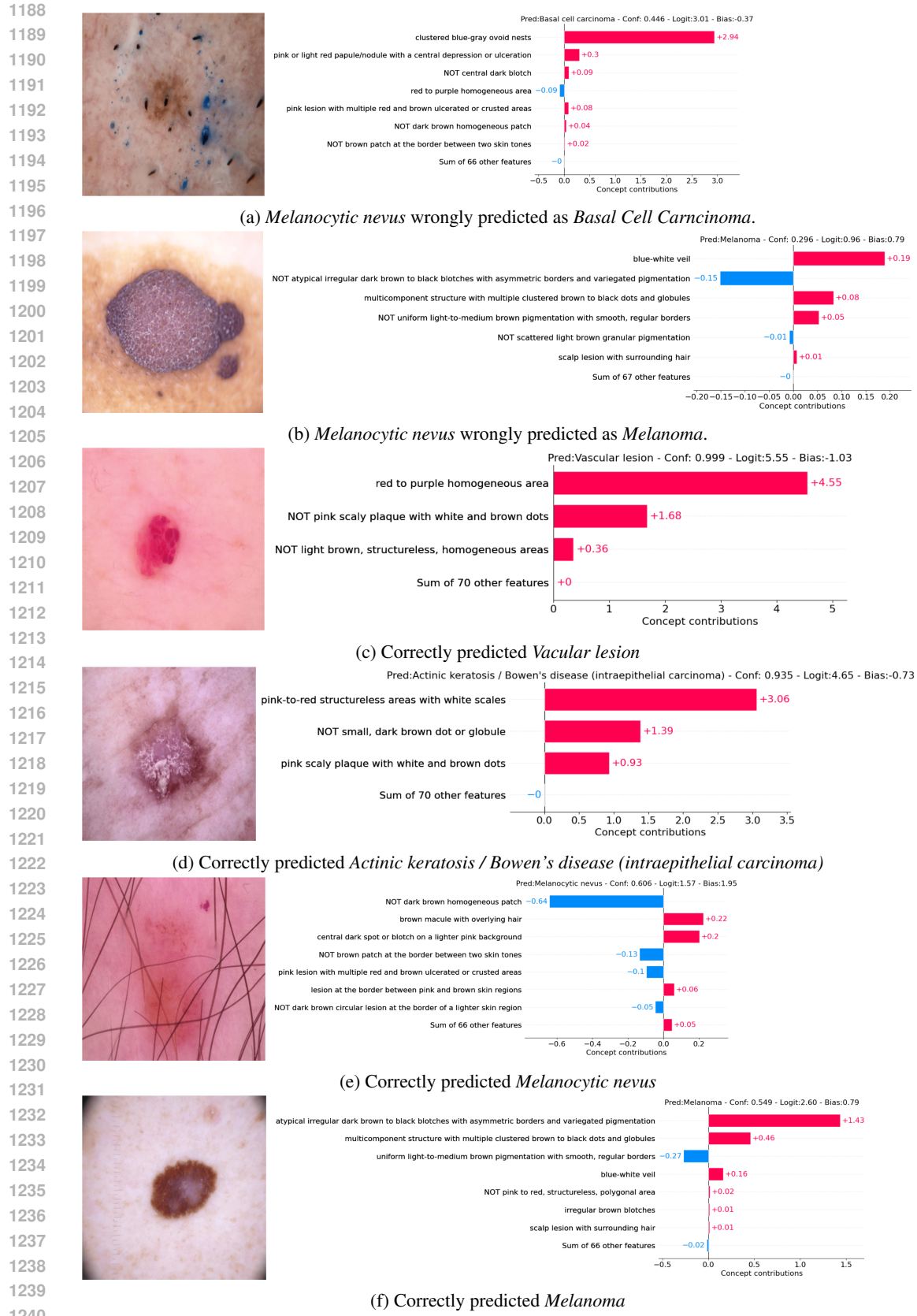


Figure 12: Examples of local explanations from ISIC2018 test set.

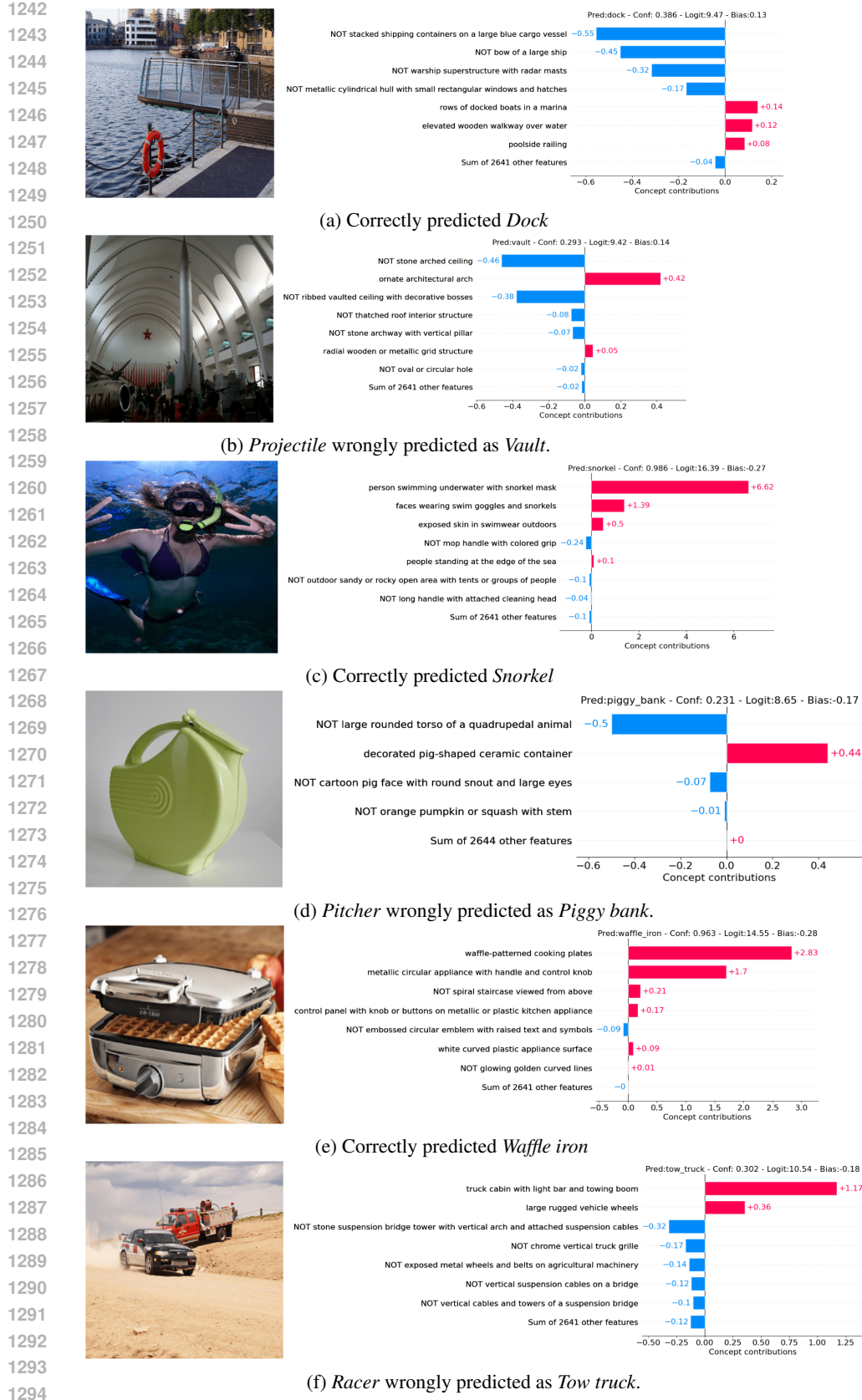


Figure 13: Examples of local explanations from ImageNet test set.

1296 **G ADDITIONAL EXPERIMENTS ON DATASET ANNOTATION**  
1297

1298 **On the effect of the reference set for annotation quality.** Our annotation pipeline provides the  
1299 MLLM with a reference set of active examples for the target concept before asking it to annotate  
1300 new samples. The goal is to visually ground the concept, which can be especially important when  
1301 the textual label alone may not be precise enough (e.g., long tail, rufous crown, or small nevus).  
1302 To quantitatively assess how much this reference set contributes to annotation quality, we use the  
1303 human-annotated concept labels available for the CUB dataset and compare the MLLM’s perfor-  
1304 mance with and without providing the reference images. For each concept, we run two parallel  
1305 annotations over the same set of randomly selected 25 images: (i) one where the model is first  
1306 shown 25 positive examples of the concept, and (ii) one where the model sees only the concept  
1307 name and the images to annotate. Ground-truth concept labels from CUB allow us to compute accu-  
1308 racy in each condition. Of the 312 CUB attributes, we exclude 19 concepts that contain fewer than  
1309 50 positive examples, leaving 293 concepts for evaluation for a total of 7325 images to be annotated.  
1310 Across these concepts, providing the reference grid achieves a measurable improvement as accuracy  
1311 increases from 65.91% (without reference) to 69.46 % (with reference images). This shows that the  
1312 MLLM effectively leverages the visual examples for better annotation. However, it is important to  
1313 note that these numbers may not be representative of the absolute annotation quality, given that CUB  
1314 concept annotations are known to be very noisy. As noted by Koh et al. (2020), each attribute was  
1315 annotated by a single non-expert crowdworker, and many concepts are fine-grained or subjective  
1316 (e.g., red belly vs rufous belly). While such inconsistencies limit the maximum attainable accuracy,  
1317 the relative improvement provides evidence in favor of the reference set being helpful in improving  
1318 the quality of the annotations.

1319 **Grid vs single-image for dataset annotation.** In the main annotation pipeline, we present the  
1320 MLLM with a  $5 \times 5$  grid of images 25 images at once, asking it to output a list of binary predictions  
1321 corresponding to each image. This batch style strategy is critical for keeping annotation costs man-  
1322 ageable, especially for large datasets such as ImageNet. However, it is natural to ask whether the  
1323 MLLM would produce higher quality annotations if instead queried with one image at a time. To  
1324 investigate this, we repeat the experiment described in the previous section, but modify the prompt-  
1325 ing so that each image is shown individually. For every concept, the model receives the same visual  
1326 reference examples, but is presented with each of the 25 test images in separate calls. We compare  
1327 the resulting accuracy with the grid-based setup.

1328 The single image approach has an accuracy of 74.0%, compared to 69.46% for the grid. This  
1329 indicates that the MLLM indeed benefits from focusing on one image at a time, likely because it  
1330 reduces cross-image interference and allows the model to allocate all attention to the visual details  
1331 of a single example. In principle, this also suggests that prompting granularity is an important  
1332 design dimension in MLLM-based annotation systems. However, the practical implications of this  
1333 improvement are highly limited. The single-image method increases the number of model calls  
1334 by a factor of 25, as each of the 25 images in the original batch now requires its own MLLM  
1335 request. As an example, for ImageNet this would increase annotation time from days to months and  
1336 the API cost from USD 370 to USD 9250. As a result, while the single-image approach achieves  
1337 better annotations, it is currently impractical for most applications. Nevertheless, these findings are  
1338 encouraging, as they indicate that as MLLMs become more cost-efficient, single-image prompting  
1339 would be a straightforward way to improve results further.

1340 **Robustness of MLLM annotation under reference set poisoning.** Providing a set of reference  
1341 images for a target concept generally improves annotation quality, but a potential risk is that if this  
1342 reference set is noisy (i.e., containing some images that represent different features than the concept),  
1343 the MLLM might inadvertently internalize these spurious visual features and associate them with the  
1344 concept. To test whether our annotation pipeline is susceptible to this effect, we design a controlled  
1345 poisoning experiment in which the reference images for a concept are deliberately contaminated  
1346 with images from a different concept. We then also contaminate the batch of images to be annotated  
1347 with images from this secondary concept and measure whether these poisoned images are predicted  
1348 as positive more often than typical negative examples. This setup provides a direct quantitative  
1349 assessment of whether the MLLM forms spurious visual associations from the reference examples  
or remains faithful to the intended concept semantics. The experiment is carried out on the CUB  
dataset, where ground-truth concept annotations allow measurement of false positive behavior.

1350 For each target concept  $A$ , we construct two types of negative examples: (i) *standard negatives* (im-  
 1351 ages that do not contain  $A$ ) and (ii) *poisoned negatives* (images that do not contain  $A$  but do contain  
 1352 a different concept  $B$ ). For every concept  $A$ , we randomly select a concept  $B$  and contaminate its  
 1353 reference set by replacing 5 out of the 25 reference images with poisoned negatives. Then, during  
 1354 annotation, we also replace 1 standard negative image per annotation batch with a poisoned nega-  
 1355 tive. The remaining pipeline is kept unchanged. We repeat this procedure for all 293 concepts with  
 1356 sufficiently many positive samples and annotate 25 images per concept, resulting in 293 MLLM  
 1357 annotation calls and a total of 7325 images.

1358 After annotation, we compute the False Positive Rate (FPR) separately for poisoned negatives and  
 1359 for standard negatives, quantify the difference using Cohen’s  $h$  effect size, and test whether the two  
 1360 proportions differ significantly using a two-proportion  $z$ -test. Results are reported in Table 6. The  
 1361 results reveal only a small difference between the FPR of poisoned and normal negatives: 0.232 vs  
 1362 0.198. The corresponding effect size, Cohen’s  $h = 0.084$ , is well below the conventional threshold  
 1363 for a “small” effect ( $h = 0.2$ ), indicating that the magnitude of this difference is tiny and negligible in  
 1364 practical terms. Consistently, the two-proportion  $z$ -test rejects the hypothesis that the two FPRs are  
 1365 different ( $p$ -value = 0.157), meaning that the observed effect is statistically indistinguishable from  
 1366 random variation. Taken together, these findings suggest that the MLLM does not meaningfully  
 1367 internalize the spurious visual features introduced through reference-set poisoning. Even when 20%  
 1368 of the reference examples are deliberately contaminated with a conflicting concept, the model’s  
 1369 annotation behavior remains largely stable, indicating that the annotation is primarily guided by the  
 1370 semantic description of the target concept rather than incidental correlations present in the reference  
 1371 examples.

1372 Table 6: Results of MLLM-based concept annotation under poisoning of the reference set on the  
 1373 CUB dataset using human-annotated concepts as ground truth. We report the false positive rates  
 1374 (FPR) for poisoned vs normal negative examples, the two-proportion  $z$ -test, and the effect size  
 1375 (Cohen’s  $h$ ).

Metric	Value
FPR (poisoned)	0.232
FPR (normal)	0.198
Two-proportion $z$ -test ( $p$ -value)	0.157
Cohen’s $h$ effect size	0.084

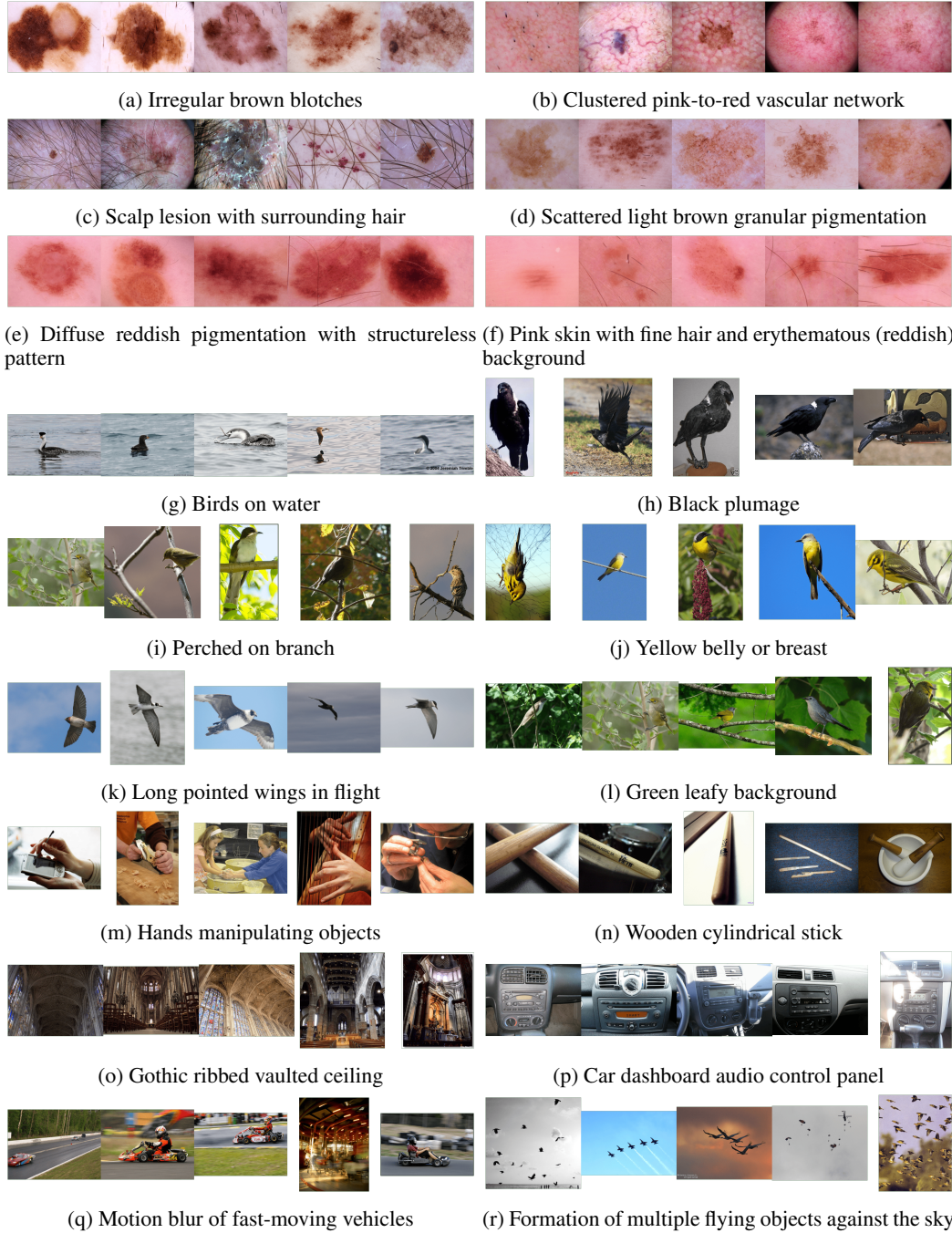
## H ACCURACIES UNDER NEC

1386 In this section, we report M-CBM accuracies when controlling for NEC instead of NCC. For context,  
 1387 NEC measures the average number of non-zero classifier weights per class (e.g., NEC=5 means that,  
 1388 on average, 5 concepts per class have non-zero weights), while NCC is defined in detail in Section 4  
 1389 and intuitively measures how many concepts, on average, are needed to explain a prediction. NCC  
 1390 can be viewed as a generalization of NEC, as when the coverage level is set to  $\tau = 1$ , NCC reduces  
 1391 to NEC (see Section H.1 for proof). Because we use a relatively high coverage level  $\tau = 0.95$ , the  
 1392 resulting accuracies are not dramatically different (see Table 7). Intuitively, NCC differs from NEC  
 1393 in that it measures sparsity at the decision-level using concept contributions (weights multiplied by  
 1394 activations), rather than just weights. This relaxes the hard cap that NEC implicitly imposes on the  
 1395 effective concept vocabulary. Indeed, with  $\text{NCC}_\tau = 5$ , the model may assign non-zero weights to  
 1396

1397 Table 7: Accuracy results at NEC=5 and NEC=avg.  
 1398

Dataset	CUB		ISIC2018				ImageNet	
Metrics	Accuracy		Accuracy		Balanced Accuracy		Accuracy	
Sparsity	NEC=5	NEC=avg	NEC=5	NEC=avg	NEC=5	NEC=avg	NEC=5	NEC=avg
M-CBM	72.54%	73.70%	69.38%	73.47%	68.97%	70.45%	71.23%	73.00%

1404  
 1405 many concepts, as long as only about 5 concepts are required, on average, to explain each prediction  
 1406 at coverage level  $\tau$ . For instance, M-CBM at NCC=5 has 271 concepts with non-zero weights on  
 1407 CUB, 47 on ISIC2018, and 2572 on ImageNet, while at NEC=5 it has 253 on CUB, 29 on ISIC2018,  
 1408 and 2343 on ImageNet. In Figure 14, we provide some examples of concepts that are used by the  
 1409 NCC=5 model but not by the NEC=5 model.  
 1410  
 1411



1422  
 1423 Figure 14: Top-5 activating images for CBL neurons that have all zero weights at NEC=5, but not  
 1424 at NCC=5 for all datasets.  
 1425  
 1426  
 1427  
 1428  
 1429  
 1430  
 1431  
 1432  
 1433  
 1434  
 1435  
 1436  
 1437  
 1438  
 1439  
 1440  
 1441  
 1442  
 1443  
 1444  
 1445  
 1446  
 1447  
 1448  
 1449  
 1450  
 1451  
 1452  
 1453  
 1454  
 1455  
 1456  
 1457

1458 H.1 RELATIONSHIP BETWEEN NEC AND NCC  
14591460 We now formalize the connection between NEC and NCC at  $\tau = 1$ .1461 **Proposition H.1.** *Let*

1462 
$$\text{NEC}(\mathbf{W}_F) = \frac{1}{C} \sum_{r=1}^C \sum_{k=1}^K \mathbf{1}\{[\mathbf{W}_F]_{k,r} \neq 0\},$$
  
1463  
1464

1465 and let  $\text{NCC}_\tau$  be defined as in Section 4. Assume that whenever  $[\mathbf{W}_F]_{k,r} \neq 0$ , the corresponding  
1466 concept logit  $[g(\mathbf{a}^{(i)})]_k$  is non-zero for all images  $i$ . This assumption is reasonable, since concept  
1467 logits are continuous,  $z$ -normalized values, so the probability of encountering an exact zero is neg-  
1468 ligible at machine precision. Then  
1469

1470 
$$\text{NCC}_1 = \text{NEC}(\mathbf{W}_F).$$
  
1471

1472 *Proof.* By definition in Section 4,

1473 
$$u_{k,r}^{(i)} = |[g(\mathbf{a}^{(i)})]_k [\mathbf{W}_F]_{k,r}| \geq 0.$$
  
1474

1475 If  $[\mathbf{W}_F]_{k,r} = 0$ , then  $u_{k,r}^{(i)} = 0$  for all  $i$ . Under our assumption, if  $[\mathbf{W}_F]_{k,r} \neq 0$ , then  $[g(\mathbf{a}^{(i)})]_k \neq 0$   
1476 for all  $i$ , hence  $u_{k,r}^{(i)} > 0$  for all  $i$ . Thus, for fixed  $r$ ,  
1477

1478 
$$u_{k,r}^{(i)} > 0 \iff [\mathbf{W}_F]_{k,r} \neq 0 \text{ for all } i.$$
  
1479

1480 For each class  $r$ , define  
1481

1482 
$$m_r = \sum_{k=1}^K \mathbf{1}\{[\mathbf{W}_F]_{k,r} \neq 0\},$$
  
1483  
1484

1485 the number of concepts with non-zero weight for class  $r$ . For any image  $i$ , exactly  $m_r$  of the  $u_{k,r}^{(i)}$   
1486 are strictly positive and the remaining  $K - m_r$  contributions are zero.  
14871488 Let  $u_{(1),r}^{(i)} \geq \dots \geq u_{(K),r}^{(i)}$  be the sorted contributions. Sorting moves the  $m_r$  positive terms to the  
1489 front, so  
1490

1491 
$$\sum_{k=1}^K u_{k,r}^{(i)} = \sum_{s=1}^{m_r} u_{(s),r}^{(i)}$$
  
1492  
1493

1494 and  $u_{(s),r}^{(i)} = 0$  for all  $s > m_r$ .  
14951496 By the definition of  $\kappa_r^{(i)}(1)$  in Section 4, it is the smallest number of top-ranked contributions whose  
1497 sum matches the total contribution  $\sum_{k=1}^K u_{k,r}^{(i)}$ . Since this total is exactly the sum of the  $m_r$  strictly  
1498 positive terms and all remaining terms are zero, it follows that  
1499

1500 
$$\kappa_r^{(i)}(1) = m_r \text{ for all } i, r.$$
  
1501

1502 Substituting into the definition of  $\text{NCC}_1$ ,  
1503

1504 
$$\text{NCC}_1 = \frac{1}{|\mathbb{D}|C} \sum_{i,r} \kappa_r^{(i)}(1) = \frac{1}{|\mathbb{D}|C} \sum_{i,r} m_r = \frac{1}{C} \sum_{r=1}^C m_r$$
  
1505  
1506

1507 Using the definition of  $m_r$ ,  
1508

1509 
$$\text{NCC}_1 = \frac{1}{C} \sum_{r=1}^C \sum_{k=1}^K \mathbf{1}\{[\mathbf{W}_F]_{k,r} \neq 0\} = \text{NEC}(\mathbf{W}_F),$$
  
1510  
1511

1512 which completes the proof.  $\square$

## 1512 I VISUALIZING SAE FEATURES

1514 In Figures 15, 17, and 16 we show the top-5 activating images for SAE neurons on CUB, ISIC2018,  
 1515 and ImageNet, respectively. We also provide their respective description given by the MLLM. These  
 1516 visualizations qualitatively assess whether the MLLM descriptions align with the neuron behavior.  
 1517 We also overlay the activating images with their respective saliency map to show where that neuron  
 1518 was looking.



1563 Figure 15: Top-5 activating images for SAE features in CUB

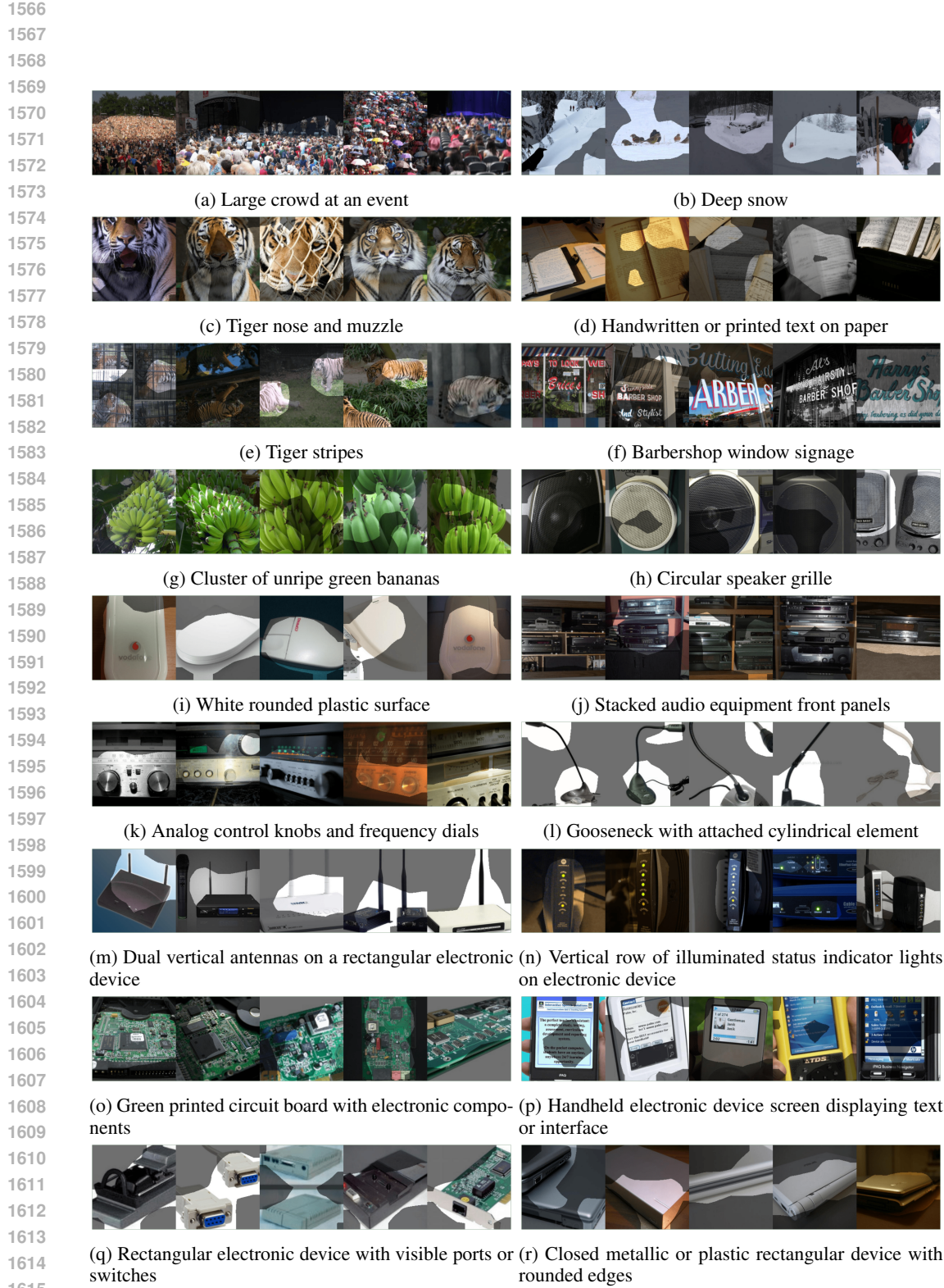


Figure 16: Top-5 activating images for SAE features in ImageNet



Figure 17: Top-5 activating images for SAE features in ISIC2018

1674  
1675  
1676  
1677  
1678  
1679  
1680  
1681  
1682  
1683

Ground Truth: **Bridegroom**1684  
1685  
1686  
1687  
1688  
1689  
1690  
1691  
1692  
1693  
1694  
1695  
1696  
1697  
1698  
1699  
1700  
1701  
1702  
1703  
1704  
1705  
1706  
1707  
1708  
1709  
1710  
1711  
1712  
1713  
1714  
1715  
1716  
1717  
1718  
1719  
1720  
1721  
1722  
1723  
1724  
1725  
1726  
1727

**M-CBM (Ours)**

Predicted: **Bridegroom** (Conf. 0.753)

- 1. bride in white wedding dress holding bouquet (+4.07)
- 2. group\_of\_people\_in\_celebratory\_or\_formal\_attire (+2.06)
- 3. men's suit jacket with dress shirt and necktie (+1.62)
- 4. wedding dress bodice and upper skirt (+1.27)
- 5. standing person in formal or distinctive clothing (+0.46)
- 6. Sum of all 2643 other concepts (+0.26)

**DN-CBM<sub>ViT</sub>**

Predicted: **Bridegroom** (Conf. 0.948)

- 1. bridal (+6.42)
- 2. couple (+2.05)
- 3. beijing (+1.12)
- 4. suits (+0.3)
- 5. parties (+0.17)
- 6. Sum of all 4091 other concepts (+0.1)

**LF-CBM**

Predicted: **Bridegroom** (Conf. 0.135)

- 1. a wedding (+4.34)
- 2. waiting at the altar (+0.55)
- 3. groom (+0.35)
- 4. Sum of all 4520 other concepts (0.0)

Figure 18: ImageNet Dataset

Ground Truth: **Great Grey Shrike**1710  
1711  
1712  
1713  
1714  
1715  
1716  
1717  
1718  
1719  
1720  
1721  
1722  
1723  
1724  
1725  
1726  
1727

**M-CBM (Ours)**

Predicted: **Great Grey Shrike** (Conf. 0.70)

- 1. black mask across eyes (+4.64)
- 2. gray body with white underparts (+1.75)
- 3. white wingbars on gray wings (+1.6)
- 4. dark cap with pale cheek (+0.3)
- 5. light gray body, black wings (+0.23)
- 6. Sum of all 273 other concepts (0.0)

**VLG-CBM<sub>CA</sub>**

Predicted: **Great Grey Shrike** (Conf. 0.41)

- 1. NOT red shoulders (+1.8)
- 2. NOT stocky body (+1.35)
- 3. NOT large black spider (+0.88)
- 4. NOT small blue green body (+0.77)
- 5. long black and white tail (+0.6)
- 6. Sum of all 530 other concepts (+0.85)

**LF-CBM**

Predicted: **Great Grey Shrike** (Conf. 0.08)

- 1. black cap and white "eyeline" (+1.51)
- 2. a white breast (+1.48)
- 3. white and black coloration (+0.9)
- 4. a white face and underparts (+0.11)
- 5. Sum of all 204 other concepts (0.0)

**DN-CBM<sub>ViT</sub>**

Predicted: **Scissor tailed Flycatcher** (Conf. 0.09)

- 1. colors (+0.62)
- 2. kramer (+0.48)
- 3. field (+0.46)
- 4. beige (+0.45)
- 5. flea (+0.42)
- 6. Sum of all 4091 other concepts (+0.05)

Figure 19: CUB Dataset

1728

1729

1730

1731

1732

1733

1734

1735

1736

1737

1738

1739

1740

1741

1742

1743

1744

1745

1746

1747

1748

1749

1750

1751

1752

1753

1754

1755

1756

1757

1758

1759

1760

1761

1762

1763

1764

1765

1766

1767

1768

1769

1770

1771

1772

1773

1774

1775

1776

1777

1778

1779

1780

1781

Ground Truth: **Melanoma****M-CBM (Ours)**Predicted: **Melanoma (Conf. 0.70)**

1. atypical irregular dark brown to black blotches with asymmetric borders and variegated pigmentation (**+5.0**)
2. NOT uniform light-to-medium brown pigmentation with smooth, regular borders (**+1.03**)
3. blue-white veil (**+0.76**)
4. multicomponent structure with multiple clustered brown to black dots and globules (**+0.75**)
5. NOT scattered light brown pigmentation (**-0.03**)
6. Sum of all 68 other concepts (**0.0**)

**LF-CBM**Predicted: **Vascular lesion (Conf. 0.54)**

1. NOT dryness or scaling (**+1.16**)
2. NOT hair follicles (**+1.09**)
3. NOT Bleeding (**-0.38**)
4. NOT Scaly or crusted surface (**+0.07**)
5. NOT Epidermis and dermis layers (**+0.01**)
6. Sum of all 30 other concepts (**0.0**)

**VLG-CBM<sub>CA</sub>**Predicted: **Melanoma (Conf. 0.45)**

1. cancer (**+1.17**)
2. redness erythema (**+0.75**)
3. NOT sun damaged skin (**-0.19**)
4. scaly or rough patches (**+0.14**)
5. NOT scaly or crusted surface (**-0.12**)
6. pathological entity (**+0.08**)
7. ulceration in some cases (**+0.08**)
8. Sum of all 73 other concepts (**+0.05**)

**DN-CBM<sub>ViT</sub>**Predicted: **Melanoma (Conf. 0.17)**

1. magnesium (**+0.05**)
2. ted (**+0.03**)
3. Sum of all 4094 other concepts (**0.0**)

Figure 20: ISIC Dataset